HHS Public Access

Author manuscript

Immunity. Author manuscript; available in PMC 2020 June 18.

Published in final edited form as:

Immunity. 2019 June 18; 50(6): 1425–1438.e5. doi:10.1016/j.immuni.2019.04.019.

Tissue-resident group 2 innate lymphoid cells differentiate by layered ontogeny and *in situ* perinatal priming

Christoph Schneider[1,#], **Jinwoo Lee**[1,#], **Satoshi Koga**[1], **Roberto R. Ricardo-Gonzalez**[1], **Jesse C. Nussbaum**[1,4], **Lucas K. Smith**[3], **Saul A. Villeda**[1], **Hong-Erh Liang**[1], **Richard M. Locksley**[1,2,3,*]

[(1)]Department of Medicine, University of California San Francisco, San Francisco, California 94143-0795, USA.

[(2)]Department of Microbiology & Immunology, University of California San Francisco, San Francisco, California 94143-0552, USA.

[(3)]Howard Hughes Medical Institute, University of California San Francisco, San Francisco, California.

[(4)]Current position: Merck Research Labs, South San Francisco, California 94080, USA.

SUMMARY

The perinatal period is a critical window for distribution of innate tissue-resident immune cells within developing organs. Despite epidemiologic evidence implicating early life environment in risk for allergy, temporally controlled lineage-tracing of group 2 innate lymphoid cells (ILC2s) during this period remains unstudied. Using complementary fate-mapping approaches and reporters for ILC2 activation, we show that ILC2s appeared in multiple organs during late gestation like tissue macrophages, but unlike the latter, a majority of peripheral ILC2 pools were generated *de novo* during the postnatal window. This period was accompanied by systemic ILC2 priming and acquisition of tissue-specific transcriptomes. Although perinatal ILC2s were variably replaced across tissues with age, the dramatic increases in tissue ILC2s following helminth infection were mediated through local expansion independent of *de novo* generation by bone marrow hematopoiesis. We provide comprehensive temporally controlled fate-mapping of an innate lymphocyte subset with notable nuances as compared to tissue macrophage ontogeny.

[*]Corresponding Author / Lead Contact: Dr. Richard M. Locksley, University of California, San Francisco, 513 Parnassus Ave, S-1032B, San Francisco, CA 94143-0795, Telephone: 415-476-5859; FAX: 415-502-5081, richard.locksley@ucsf.edu.

AUTHOR CONTRIBUTIONS

C.S. and J.L. conceived the study, designed and performed experiments, analyzed data and wrote the manuscript with R.M.L. H.-E.L. designed the *Arg1*[RFP-CreERT2] reporter cassette and performed the embryonic stem cell work. H.-E.L., S.K., R.R.R-G. and J.C.N. assisted with additional experiments. L.K.S. and S.A.V. assisted with parabiosis experiments. R.M.L. directed the study and wrote the paper with C.S. and J.L.

[#]These authors contributed equally to this work.

DECLARATION OF INTERESTS

The authors declare no competing interests.

Graphical Abstract

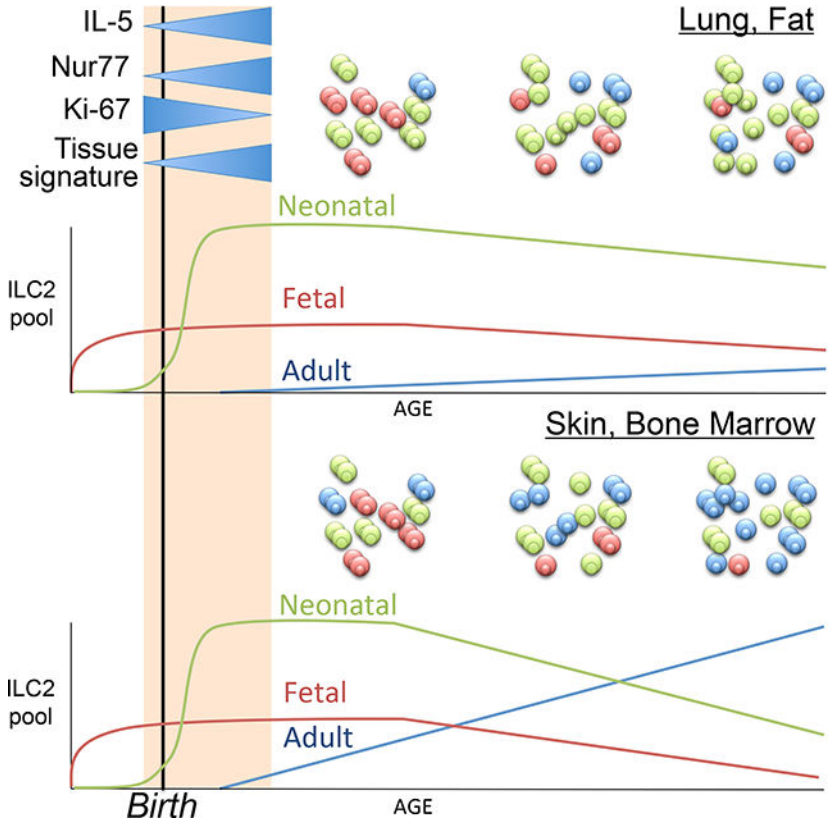

eTOC blurb

The perinatal period is critical for distribution of innate tissue-resident immune cells within developing organs. Using temporally controlled fate-mapping of group 2 innate lymphoid cells (ILC2s) Schneider and colleagues demonstrate that the neonatal period is accompanied by *de novo* ILC2 generation, systemic effector repertoire activation and acquisition of tissue-specific signatures.

Keywords

ILC2s; ontogeny; Arginase-1; Id2; allergy; fate-mapping; IL-5; type 2 cytokines

INTRODUCTION

Asthma and allergic diseases represent a major health burden worldwide (Pawankar et al., 2011). Epidemiologic evidence has increasingly linked various environmental exposures during early years of life with the risk of developing allergies (Lambrecht and Hammad, 2017). The discovery of group 2 innate lymphoid cells (Moro et al., 2010; Neill et al., 2010; Price et al., 2010), or ILC2s, which express type 2 cytokines in the absence of antigen receptors, offers an opportunity to look for functions of these cells independent of traditional host immune defense in efforts to reveal the contextual roots of allergic immunity. Indeed,

activation of these cells by a variety of epithelial cytokines, neuropeptides and eicosanoids, and involvement in metabolism, tissue repair, and remodeling in multiple organs, have begun to outline a previously unsuspected role for type 2 immunity integrated deeply into aspects of basal homeostasis (Ebbo et al., 2017; Klose and Artis, 2016; Kotas and Locksley, 2018). Further understanding could be gained by examining the development, activation and turnover of these cells in tissues, particularly during early life when environmental inputs might be critical.

Temporally restricted *in vivo* lineage-tracing has accelerated our understanding of hematopoietic development from the conventional model that all leukocytes arise from bone marrow (BM) hematopoietic stem cells (HSCs) to the current model that progressive waves of immune cell generation begin in early development. In the macrophage field in particular, fate-mapping studies have replaced the dogma that tissue-resident macrophages rely on constant replenishment from blood monocytes for homeostasis (van Furth and Cohn, 1968) with the discovery that recurrent waves of precursor cells—from early embryonic yolk sac macrophages, from late embryonic fetal monocytes, and from adult blood monocytes—layer together in differing proportions to comprise the tissue resident macrophage pool in different organs (McGrath et al., 2015; Perdiguero and Geissman, 2016). The ability to distinguish cells based on ontogeny has revealed unsuspected transcriptomic and epigenomic landscapes that differ among macrophages of different origins, whether from fetal hematopoiesis in the yolk sac and liver or from adult hematopoiesis in the BM (Gibbings et al., 2015; Lavin et al., 2014). ILC progenitors with the capacity to give rise to mature ILCs *in vitro* and *in vivo* after transfer into lymphopenic mice have been identified in fetal tissues (Bando et al., 2015; Ishizuka et al., 2016) and in adult BM (Constantinides et al., 2014; Hoyler et al., 2012; Klose et al., 2014), but the relative contributions of these populations and their turnover among adult tissue ILC2 pools remain poorly studied, in part due to the lack of tools to reliably fate-map and track these cells.

The development of innate lymphoid cells requires the transcriptional regulator Id2 (Boos et al., 2007; Moro et al., 2010; Yokota et al., 1999), and high Id2 expression is maintained in mature innate lymphoid cells (Hoyler et al., 2012). Putative ILC precursors that express Id2 are present in the BM (Constantinides et al., 2014; Klose et al., 2014), providing a potential source for these cells. ILC precursors that express the urea cycle enzyme Arg1 have also been identified in the small intestine before birth (Bando et al., 2015), which suggests that ILCs can seed tissues prenatally and might arise from fetally-generated precursors. Parabiosis experiments revealed minimal replacement of tissue ILC2s by circulating cells under steady-state conditions (Gasteiger et al., 2015; Moro et al., 2016), implying little contribution from bloodborne precursors, and consistent with the designation of ILC2s as predominantly tissue-resident cells (Fan and Rudensky, 2016). Limitations and variability driven by the duration of parabiosis (Gasteiger et al., 2015; Huang et al., 2018) suggest that complementary approaches will be necessary to comprehensively assess contributions by cells that might be derived during different phases of development.

In this study, we have used *Arg1*-driven and *Id2*-driven fate-mapping strategies together with transcriptome profiling to assess the ontogeny and turnover of ILC2s in mouse tissues over the period from prenatal tissue seeding to adulthood in order to clarify the origins and

lifespans of these cells in tissues, and to gain greater understanding of the role of ILC2s in local and systemic contributions to type 2 immunity. Our studies reveal three distinct waves of ILC2 development characterized by dispersal into tissues, expansion and activation of tissue-specific transcriptional programs, and maintenance, with evidence for niche-specific differences in local regulation of survival and turnover throughout life.

RESULTS

Tissue ILC2s are replaced by newly generated ILC2s at a low rate

We used two independent tamoxifen-inducible Cre mouse strains to lineage-trace ILC2s and to assess their temporal origin. First, we generated an *Arg1*$^{\text{RFP-CreERT2}}$ mouse strain, in which expression of red fluorescent protein (RFP) as well as tamoxifeninducible Cre (CreERT2) is under the control of the endogenous arginase-1 (*Arg1*) promoter (Fig. 1A). Consistent with previous reports (Bando et al., 2013, 2015; Monticelli et al., 2016), *Arg1*$^{\text{RFP-CreERT2}}$ mice accurately report *Arg1* expression in CD25^{+}Id2$^{\text{GFP+}}$ ILC2s from the BM, lung, and adipose tissue (Supp. Fig. 1A,B). In contrast, *Arg1* expression was absent in CD25^{-}Id2$^{\text{GFP+}}$ BM ILC precursors (CHILPs), in a fraction of ILC2s from the small intestine lamina propria (Supp. Fig. 1A,B) (Schneider et al., 2018), and in a majority of the ILC2s in the skin (Supp. Fig. 1C–E), corroborating heterogeneity in *Arg1* expression among mature ILC2 subsets in different tissues (Ricardo-Gonzalez et al., 2018). In addition to ILC2s, the *Arg1* reporter was expressed by a subset of small intestinal RORγt^{+} ILC3s (Bando et al., 2015; Robinette et al., 2015) and in F4/80$^{\text{hi}}$MHCII$^{\text{low}}$ peritoneal macrophages (Supp. Fig. 1A,F). Due to the absence of *Arg1* expression in ILC2s of certain tissues, and as a second and independent approach, we used a previously described *Id2*-CreER$^{\text{T2}}$ genetically targeted mouse (Rawlins et al., 2009), to compare and confirm results obtained using the *Arg1*$^{\text{RFP-CreERT2}}$ strain.

To assess the turnover of adult ILC2s, we crossed these two strains to R26REYFP or R26R-RFP reporter mice for fate-mapping. Adult mice were fed tamoxifen diet for 4 weeks to enable activation of the floxed reporter allele, and then analyzed monthly for 4 months after return to chow diet (Fig. 1B,C). Notably, the BM ILC2 population was steadily diluted by newly generated unlabeled cells, as assessed by the decreasing proportion of fate-mapped cells in both strains of mice (Fig. 1D). By 2–3 months after tamoxifen removal, fewer than half of BM ILC2s remained fate-mapped. Despite the dilution of ILC2s in the BM, there was minimal change in labeling frequency of tissue ILC2 populations over the course of 4 months following removal from tamoxifen (Fig. 1E) with the exception of the skin (Fig. 1F), suggesting a slow rate of tissue ILC2 replenishment, or expansion through *de novo* generation from a non-fate-mapped population. To address whether changes in the size of ILC2 pools could contribute to the dilution of fate-mapping labeling in certain tissues, we determined the absolute numbers at distinct ages (2, 4, 6 months). Notably, total ILC2 numbers gradually increased in the BM and skin, which showed the highest rate of fate-mapping label dilution (Supp. Fig. 1G). In contrast, the numbers of ILC2s in the lung and VAT remained relatively stable over the same period of 4 months, consistent with little dilution of the percentages of fate-mapped cells in these organs. These results suggest that the differential decay in ILC2 fate-mapping frequencies might, at least in part, be caused by

addition of *de novo* generated ILC2s to the pools of existing ILC2s, rather than replacement of the latter. Taken together, these data are consistent with generally stable long-lived populations of ILC2s in most adult tissues, but with more rapid turnover and continuous expansion of the ILC2 pools in BM and skin.

Tissue ILC2s do not recirculate or repopulate empty niches at steady state

To assess further the homeostatic turnover of tissue ILC2s, we performed parabiosis experiments in which CD45.1 mice carrying an *Arg1*-YFP reporter allele (Yarg) were surgically conjoined with CD45.2 WT mice (Fig. 2A). After 5 weeks, the lungs and spleens of wild-type recipients contained approximately equivalent numbers of $CD4^+$ T cells and eosinophils derived from each parabiont, indicating the free exchange of these circulating cells across the surgical anastomosis (Fig. 2B, Suppl. Fig. 2A,B**)**. However, consistent with previous reports over similar periods (Gasteiger et al., 2015; Huang et al., 2018; Moro et al., 2016), lung ILC2s showed <5% crossover between the paired mice, corroborating a relatively long tissue lifespan and limited replenishment from the circulation (Fig. 2C, Suppl. Fig. 2C). Because niche occupancy in the WT mice may have prevented circulating progenitors from engrafting between the parabionts, we also tested the ability of ILC2s to reconstitute IL-7Rα-deficient recipients, which lack ILCs, B cells, and T cells. Although the percentage of parabiont-derived ILC2s was higher in the IL-7Rα-deficient host (Fig. 2D–F), perhaps due to increased niche availability and/or the presence of uncontested growth factors, including IL-7, the total number of ILC2s was still substantially below those in *Arg1*-YFP (IL-7Rα-sufficient) hosts (Fig. 2D), confirming that ILC2s are predominantly long-lived tissue-resident cells, which maintain themselves during adulthood largely independent from replenishment by rare circulating precursors. We observed the same patterns of replacement when assessing ILC2s in the adipose tissue and in the small intestine lamina propria **(**Supp. Fig. 2D,E**)**, and thus extend prior observations using these types of approaches (Gasteiger et al., 2015; Huang et al., 2018; Moro et al., 2016). To assess the possibility that an inherently impaired niche in the lymphopenic IL-7Rα-deficient parabionts may have prevented engraftment of circulating cells, we quantified the number of ILC2-supporting mesenchymal cells (Dahlgren et al., 2019; Koga et al., 2018) in $Il7r^{-/-}$ mice. The frequency and number of $PDGFR\alpha^+gp38^+$ stromal cells in the lung, and their expression of important niche factors, IL-33 and thymic stromal lymphopoietin (TSLP), were comparable between $Il7r^{-/-}$ and wild-type mice **(**Supp. Fig. 2F,G**)**, suggesting that the ILC2 niche is not obviously altered in these lymphopenic mice.

Prenatal ILC2 precursors seed tissues during fetal development and contribute to the adult ILC2 tissue pool

Our results using adult lineage-tracing in two independent fate-mapping strains and two conditions of parabiosis suggested that tissue ILC2 pools are established prior to reaching adulthood. Many innate tissue-resident cells, including tissue macrophages, are seeded during fetal development (Ginhoux and Guilliams, 2016), and previous work in our laboratory has characterized *Arg1*-YFP expressing ILC precursors in the fetal small intestine (Bando et al., 2015). As assessed using flow cytometry, *Arg1*-RFP^+ cells with a surface marker expression profile of mature ILC2s (e.g. Lin^-IL-$7R\alpha^+Thy1^+ST2^+$) appeared as early as embryonic day 17.5 (E17.5) in the fetal lung, small intestine, and skin (Fig. 3A). These

cells expressed GATA-3 (Fig. 3A) and Ki-67 **(**Suppl. Fig. 3A**)**, consistent with active cell proliferation.

To determine whether these fetal tissue-seeding $Arg1^+$ ILC2s contribute to adult ILC2 pools, we performed lineage-tracing experiments by administering tamoxifen prenatally during E16.5–18.5, and analyzing the labelled tissue ILC2 populations at 2 months of age (Fig. 3B). Labeling efficiency at E19.5 in lung and small intestine was robust (30–45%); however the absence of visceral adipose tissue (VAT) in the embryos and the absence of fetal BM ILC2s precluded analysis in these tissues (Fig. 3C–E). By two months post-birth, however, only a fraction (5–10%) of the ILC2s in lung, small intestine, and visceral adipose tissue (VAT) remained labeled and were thus embryonically derived (Fig. 3C,D). Proportions of the latter were greater in lung and VAT than in small intestine. Although a majority of $Gata\text{-}3^+$ ILC2s in the fetal small intestine co-expressed the subunits of the IL-33 and IL-25 receptors, ST2 and IL-17RB, only a small fraction of their adult counterparts expressed ST2 (Supp. Fig. 3B). However, the fraction of fetally-labelled cells was higher among the $ST2^+$ compared to $ST2^-$ ILC2s, suggesting differential contribution of fetal-derived $Arg1^+$ cells to the heterogenous ILC2 compartments in the adult small intestine (Fig. 3D, Supp. Fig. 3C). Notably, none of the putative ILC2 precursors (ILC2Ps) in the BM remained labeled in the adult (Fig. 3E), suggesting that post-birth BM $Arg1^+$ ILC2s have an origin temporally distinct from and with no contribution from prenatally-derived ILC2s.

Early postnatal ILC2s comprise the majority of the ILC2 pool in adult lung and VAT

We and others have noted the acute expansion and activation of ILC2s that occur in the lung shortly after birth (Huang et al., 2018; Kleer et al., 2016; Nussbaum et al., 2013; Saluzzo et al., 2017; Steer et al., 2017). Given these observations, we used lineage-tracing in *Arg1*-CreERT2 and *Id2*-CreERT2 mice to assess the contribution of early postnatal ILC2s to adult tissue ILC2 pools. At 2 weeks of age, ILC2s in the lung and small intestine express *Arg1*, in contrast to the skin, where, similar to adult mice, ILC2s expressed little *Arg1* (Fig. 4A). *Arg1*-CreERT2 and *Id2*-CreERT2 pups were given tamoxifen on postnatal days 10–12 and analyzed at various time points to assess the numbers of label-retaining ILC2s in multiple tissues (Fig. 4B,E). Notably, ILC2s in the BM were almost completely diluted and/or replenished by unlabeled cells within 2 months suggesting their continuous *de novo* generation during early BM hematopoiesis (Fig. 4C,F). In contrast, and as compared to the dilution of fetally-labeled ILC2s, a significantly higher fraction (40–70%) of fate-mapped ILC2s were present in adult lung, adipose tissues, small intestine, and skin (using *Id2*-CreERT2 mice, since *Arg1* is poorly expressed), and this was comparable in both strains of fate-mapping mice (Fig. 4C–G). There was some continuing dilution of fate-mapped ILC2s during the period between 2 and 8 weeks of age, indicating that *de novo* ILC2 generation likely continues beyond postnatal day 12, but, by 8 weeks of age, the tissue ILC2 pool remained relatively stable in the lung and VAT throughout the life of the mouse (Fig. 4D,G); this pool of fate-mapped cells persisted in mice that were over 1 year old. In contrast, in the skin and small intestine, ILC2s were replaced more rapidly by newly generated, unlabeled ILC2s, such that, by 1 year of age, only ~5% of ILC2s remained among postnatally-labeled cells (Fig. 4D,G), although postnatally-mapped cells clearly remain for many months even in these tissues. Consistently, heterogeneity was apparent in comparing the proportions of fate-

mapped and non-fate-mapped cells among the different tissues. In the small intestine, a subpopulation of KLRG1^{+}ST2^{+} ILC2s remained stable throughout adulthood, consistent with a predominant early postnatal origin for these cells (Fig. 4D).

Tissues of the newborn mouse are characterized by vigorous ILC2 activation and proliferation that is dependent on IL-7Rα signaling

Prior studies, including our own, have noted extensive proliferation and activation of ILC2s in lung that occurs around the time of birth and extends through weaning (Kleer et al., 2016; Nussbaum et al., 2013; Saluzzo et al., 2017; Steer et al., 2017). Here, we demonstrated that this neonatal wave of ILC2 expansion and activation occurred systemically, as assessed kinetically in lung, small intestine, skin, and BM (Fig. 5A). The development of ILC2s is dependent on the cytokine IL-7 (Moro et al., 2010), and we confirmed that the early expansion of ILC2s was also dependent on IL-7R signaling: prenatal administration of a blocking antibody to IL-7Rα resulted in significantly decreased ILC2 frequencies in the lungs, small intestine, and skin of neonatal mice (Fig. 5B). Despite three doses of anti-IL-7R, however, ILC2 frequencies largely recovered by 9 weeks of age in the lungs, small intestine, skin, and visceral adipose tissue (Fig. 5B), consistent with substantial restorative capacity.

Given this developmental time window for ILC2 proliferation, we assessed expression of the defining type 2 cytokines for ILC2s, IL-5 and IL-13, using previously described and validated reporter mice (Liang et al., 2012; Nussbaum et al., 2013). We found that an increasing proportion of ILC2s turned reporter-positive for IL-5 and IL-13, although much smaller in frequency for the latter, over these first weeks of life (Fig. 5C,D). Systemic opening of the *Il5* locus was coincident with proliferation in peripheral tissues, and was essentially absent among BM ILC2s (Fig. 5C). ILC2 activation during this period was not dependent on the presence of microbiota, as neither *Il5* transcript expression nor *Il13* transcript expression was decreased in ILC2s sorted from the tissues of gnotobiotic neonatal mice (Fig. 5E,F).

We previously noted high mRNA expression of the nuclear hormone receptor Nur77, or *Nr4a1*, in ILC2s isolated from peripheral tissues as compared to the BM (Fig. 5G) (Ricardo-Gonzalez et al., 2018). *Nr4a1* is an immediate early gene expressed in hematopoietic cells in association with growth factor, cytokine, inflammatory and proliferative signals, and important in mediating cell survival during stress (Maxwell and Muscat, 2006). Lymphocyte activation of adaptive T and B cells can be monitored *in situ* using cells from *Nr4a1*-GFP reporter mice, and ‘tuning’ of *Nr4a1*-GFP corresponds with the degree of integrated signals accumulating within the cell (Zikherman et al., 2012). We speculated that Nur77 expression might report the activation status of ILC2s similar to adaptive lymphocytes. Indeed, when stimulated with rIL-33 *in vivo* ILC2s in the BM and lung of *Nr4a1*-GFP mice responded with increased Nur77 reporter expression (Supp. Fig. 4A,B). We then used *Nr4a1*-GFP mice to assess whether ILC2s engage these pathways during the period of early postnatal expansion and activation. Indeed, ILC2s underwent a marked increase in *Nr4a1*-reporter expression in the early postnatal period in tissues that is maintained into adulthood (Fig. 5H); in contrast, *Nr4a1*-reporter expression remained low among ILC2s from fetal liver and

adult BM. Notably, postnatal induction of IL-5 expression in peripheral ILC2s correlated with high expression of *Nr4a1*-GFP, although analysis revealed slightly different kinetics in ILC2 priming between the different organs, including the lung, small intestine, and skin (Fig. 5I).

Tissue-specific heterogeneity of ILC2s is established in the early postnatal wave

Developing ILC2s position across tissues as they expand and activate, but how they compare to long-lived adult tissue ILC2s in their transcriptional profiles may elucidate previously unknown periods of tissue-driven differentiation. To assess this, we sorted ILC2s from 2-week-old mice and 8–14-week-old mice on the same day (to eliminate batch effects), and used single-cell RNA-sequencing analysis to assess cell and tissue heterogeneity. Early postnatal ILC2s clustered distinctly from adult ILC2s (Fig. 6A,B), and were enriched for cells showing increased transcripts associated with cellular activation (*Il5, Il13, Nr4a1, Mki67*), as compared to adult ILC2s (Fig. 6C–F and Supp. Fig. 5A–F). However, when analyzed in aggregate, early postnatal ILC2s from different tissues localized with adult ILC2s from the same tissues, and consistent with a tissue-organizing expression pattern that has already developed during the early postnatal period during the period of marked ILC2 expansion (Fig. 6G). In addition to transcripts known to be associated with ILC2 activation, certain chemokine genes (*Ccl1*, *Cxcl2*) were upregulated in the early postnatal ILC2s (Fig. 6E,F and Supp. Fig. 6A,D,G**)**, suggesting that ILC2s could play a role in the early recruitment of other immune cells into tissues. A subset of TNF superfamily gene transcripts, particularly those involved in lymphotoxin-beta receptor signaling (*Ltb, Tnfsf14*), were present in both early postnatal and adult ILC2s **(**Supp. Fig. 6B,C,E,F**)**, and although these genes were not differentially expressed in early postnatal ILC2s to a statistically significant degree, the expression of these genes further suggests a potential role for ILC2s in orchestrating processes associated with immune development. Taken together, these data demonstrate that ILC2s, although first appearing during fetal hematopoiesis, establish their presence in tissues primarily during early postnatal development during a period of rapid expansion, priming, and acquisition of tissue-defining gene-expression patterns.

Newly generated ILC2s do not contribute to ILC2 expansion accompanying migratory helminth infection

Although adult tissue ILC2s are dominated by a tissue-resident and infrequently replaced population in most tissues (Fig. 1), their dynamics during acute immune perturbations have been less carefully quantitated. We used *Nippostrongylus brasiliensis* (*N. brasiliensis*), a migratory helminth that induces a vigorous systemic type 2 immune response with marked tissue effects in both the lungs and small intestine (Camberis et al.), as underscored by a nearly 8-fold increase in ILC2 numbers (Fig. 7A,B). Using mice with postnatally fate-mapped ILC2s, we found that even after infection with *N. brasiliensis*, the proportion of fate-mapped cells showed minimal decrease in the lung, spleen, and mesenteric LN (Fig. 7B–D), despite the considerable increase in ILC2 numbers. These data suggest a minor contribution of *de novo*-generated ILC2s even in an inflammatory setting. Of note, essentially none of the putative BM ILC2 precursors were fate-mapped at the time of infection, ruling out any major contribution of ‘ILC2Ps’ to the expansion of ILC2s that

accompanies migratory helminth infection (Fig. 7E). Furthermore, we found that the differential ILC2 fate-mapping frequencies between tissues such as the lung and small intestine-draining lymph nodes were maintained after infection (Fig. 7B,D). Altogether, our studies suggest that the increases in ILC2s in the context of migratory helminth infection are predominantly mediated through local expansion of pre-existing ILC2 pools at sites of inflammation.

DISCUSSION

Using fate-mapping in combination with markers for proliferation and activation, we make several observations relevant to the understanding of ILC2 biology. First, we identified three temporally distinct origins for tissue-resident ILC2s—fetally-derived ILC2s that were distributed to tissues before birth, postnatally-derived ILC2s that were generated in the period from birth through weaning, and adult-derived ILC2s that slowly diluted the pre-existing ILC2s. Second, we showed that steady-state ILC2 replacement by *de novo* ILC2s generated in adult life was dynamic but tissue-specific, with slow turnover in lung, fat and small intestine but more rapid dilution in the BM and skin. Third, using a combination of reporter mice and single-cell transcriptomics, we have shown that the perinatal seeding of peripheral tissues coincided with the period when ILC2s expand, activate their effector repertoire, and establish a tissue-specific transcriptomic signature that remains through life (Ricardo-Gonzalez et al., 2018). Lastly, using a mouse model of helminth infection, we found that the dominant mechanism by which ILC2 numbers increase in the lung after *N. brasiliensis* infection is the expansion of pre-existing ILC2s rather than *de novo* generation of new ILC2s.

Our studies reveal that the adult tissue ILC2 pool comprises populations that are both prenatally and postnatally derived, and furthermore, that the postnatally derived population, in many tissues, arises largely within the first few weeks of life with minor contribution and replenishment by subsequent adult BM hematopoietic stem cell (HSC)-derived hematopoiesis. These findings reveal similarity between ILC2s and other innate-like lymphocytes (Carding and Egan, 2002; Montecino-Rodriguez et al., 2016), and even regulatory T (Treg) cells (Yang et al., 2015), and highlight the temporal window for niche seeding by tissue-resident immune cells in developing organs (Eberl et al., 2004; Gentek et al., 2018; Ginhoux and Guilliams, 2016; Hoeffel and Ginhoux, 2015; Sawa et al., 2010; Yang et al., 2015). Whether the early postnatal ILC2 populations identified here originate from conventional HSC-dependent BM hematopoiesis or from an alternative source, such as multipotent progenitors in the spleen (Ghaedi et al., 2016) or from progenitors already present within the tissue, requires further study.

Our fate-mapping studies also highlighted notable differences in the ontogeny of tissue macrophages and ILC2s, which both appeared in multiple organs during late gestation. Tissue macrophage populations were largely established during fetal development and derived predominantly from embryonic progenitors that originated in the yolk sac and fetal liver (Ginhoux and Guilliams, 2016). Here, we demonstrated that a majority of the peripheral ILC2 pools were generated *de novo* during a postnatal window, which diluted the proportion of fetal ILC2s, and persisted into adulthood. Whether these populations derive

from distinct progenitors, which might include fetal and adult HSCs (Beaudin and Forsberg, 2016), remains unknown. Notably, a transient wave of developmentally restricted HSCs with higher lymphoid cell production compared to fetal and adult HSCs and greater capacity to generate innate-like B and T lymphocytes has been described (Beaudin et al., 2016). In support of this, recent fate-mapping of adult HSCs revealed their minimal contribution to B-1a cells and tissue macrophage compartments, but ILCs were not analyzed (Sawai et al., 2016). The observation that these stereotyped developmental trajectories early in life appear to be conserved even in humans highlight the need for a better understanding of the perinatal dynamics in immune development (Olin et al., 2018).

Our fate-mapping approach revealed dynamic complexity underlying ILC2 turnover and dilution, which manifests striking parallels with the varying kinetics observed for macrophage turnover in different tissues, with the differences in adult HSC contribution becoming increasingly apparent with age after fate-mapping. Notably, subsets of tissue-resident macrophages in the intestine (Shaw et al., 2018) and skin (Tamoutounour et al., 2013) have higher rates of replacement compared to other tissues, including in the lung (Ginhoux and Guilliams, 2016), mirroring observations generated here for ILC2s. The intestine and skin are impacted by dietary and microbial stimuli, and undergo dynamic phases of remodeling, including continuous small intestinal epithelial renewal in the bowel and hair follicle cycling in the skin, which potentially alter existing niches or create new ones that might enable colonization by *de novo* generated ILC2s. These processes might also contribute to yet unappreciated differences in subset-specific stability within an organ, as suggested by the differential dilution kinetics between $ST2^+$ and $ST2^-$ small intestinal ILC2s. Notably, among multiple peripheral tissues, ILC2s in the small intestine and skin express the highest amounts of IL-13 (Ricardo-Gonzalez et al., 2018), a dynamic marker of ILC2 activation (Liang et al., 2012), suggesting functions devoted to homeostatic activities in these organs. Further studies will be required to determine the effect of recurring activation on ILC2 replenishment by circulating or local precursors, as well as the potential effects of increased migratory behavior as recently described for ILC2s in the small intestine following helminth infection (Huang et al., 2018). In our studies, by comparing non-fate-mapped and fate-mapped ILC2s in tissues, we found that pre-existing ILC2 pools expand in the lung after infection with *N. brasiliensis*, with minimal dilution of the pre-existing fate-mapped population by cells generated *de novo* from unlabeled local or BM precursors. However, further studies are needed to assess if ILC2s generated during different developmental waves display functional heterogeneity as described for $CD8^+$ T cells (Smith et al., 2018).

Using markers for proliferation and activation, and corroborated by single-cell transcriptomics, we have shown that the perinatal establishment of peripheral ILC2 pools corresponded with the period when ILC2s expand, begin to activate their cytokine repertoire, and establish a tissue-specific transcriptomic signature. Although previously recognized as an important time window for pulmonary ILC2 activation associated with onset of breathing (Saluzzo et al., 2017), our studies demonstrated that ILC2 expansion and activation occurs systemically, suggesting that common niche factors might be involved in shaping a core effector repertoire, including IL-5 expression. While postnatal acquisition of this primed state appeared to be conserved across all tissues analyzed, the local environment also

imprinted a tissue-defining transcriptomic signature that resembled that of adult steady-state tissue ILC2s (Ricardo-Gonzalez et al., 2018) through mechanisms that remain to be identified. Therefore, and perhaps not surprisingly, ILC2s closely resemble fetal-derived tissue macrophages not only with regard to the kinetics of their appearance, but also in their capacity to integrate into tissues and acquire organ-specific gene expression programs that are likely related to distinct functions in each tissue (Mass et al., 2016). Notably, despite clustering with their adult counterparts, our scRNA-seq analysis of postnatal ILC2s revealed differences in the expression of genes associated with activation, cell growth, chemokine production, and immune crosstalk.

Although the local signals underlying the developmental priming in the tissue remain to be determined, it is intriguing to speculate that the incipient cross-talk between ILC2s and other immune and non-immune cells during this period of organ growth and remodeling might both guide and be shaped by the gene expression programs in ILC2s. We might also speculate that similar interactions might be recapitulated later during life as part of homeostatic ILC2 activitation and during tissue perturbation. Whether modulation of this early pool of ILC2s can have long-lasting consequences for the immune tone of the tissue, as has been described for neonatal regulatory T cells (Yang et al., 2015), will be an important area for further investigation, given the increasing recognition that perturbations during the neonatal period of life can have long-term effects with regard to immune function and disease susceptibility (Gollwitzer and Marsland, 2015; Kotas and Locksley, 2018).

In summary, we have demonstrated a previously unappreciated tripartite origin for tissue-resident ILC2s. Our studies reinforce the importance of the early postnatal window for the expansion and activation of resident immune cells, and show that ILC2 replacement is dynamic and tissue-dependent, revealing evidence for local regulation that remains unexplored. Looking forward, our discoveries delineate the interventional windows of ILC2 and type 2 cytokine modulation and can inform the prognostic value of interventions in early life or even in utero, broaching the possibility of therapeutically targeting specific ILC2 subsets based on ontogeny and the tissue of residency. Our findings bring ILC2s into the larger ongoing conversation regarding the influence of ontogeny and local signals on long-lived tissue-resident immune cells, which are established early during development, and highlight the need for further studies addressing their roles during this important time-window that has been associated with risk for human allergic diseases.

STAR METHODS

CONTACT FOR REAGENT AND RESOURCE SHARING

Further information and requests for resources and reagents should be directed to and will be fulfilled by the Lead Contact, Richard M. Locksley (richard.locksley@ucsf.edu).

EXPERIMENTAL MODEL AND SUBJECT DETAILS

Mice—*Arg1*^{Yarg} (*Arg1*-YFP; B6.129S4-*Arg1*^{tm1Lky}/J; 015857) (Reese et al., 2007), *Il5*^{Red5} (Red5; B6(C)-*Il5*$^{tm1.1(icre)Lky}$/J; 030926) (Nussbaum et al., 2013), and *Il13*^{Smart} (Smart13; B6.129S4(C)-*Il13*$^{tm2.1Lky}$/J; 031367) (Liang et al., 2012) mice have been previously

described. Id2-GFP (B6.129S(Cg)-*Id2*$^{tm2.1Blh}$/ZhuJ; 016224), *Id2*^{CreERT2} (B6.129S(Cg)-*Id2*$^{tm1.1(cre/ERT2)Blh}$/ZhuJ; 016222), *R26R*^{YFP} (B6.129X1-*Gt(ROSA)26Sor*$^{tm1(EYFP)Cos}$/J; 006148), *Rorc*(γt)^{GFP} (B6.129P2(Cg)-*Rorc*^{tm2Litt}/J; 007572) and *Il7r*$^{-/-}$ (B6.129S7-*Il7r*^{tm1Imx}/J; 002295) and wild-type (C57BL/6J; 000664) mice were purchased from the Jackson Laboratory. *R26R*^{RFP} mice were provided by E. Robey (Berkeley). Nur77-GFP BAC transgene mice were provided by J. Zikherman (UCSF) (Zikherman et al., 2012).

Arg1$^{RFP\text{-}CreERT2}$ mice (*Arg1*-RFP) were generated by homologous gene targeting in C57BL/6 embryonic stem cells. In brief, the previously published plasmid pKO915-DT (Lexicon) containing the *Arg1*-YFP reporter (Reese et al., 2007), was modified to replace the eYFP and neo cassette with a tdTomato-T2A-CreERT2-frt-neo-frt sequence, such that the cassette now contained (in order from 5' to 3') encephalomyocarditis virus IRES, tandem dimer (td) Tomato, T2A self-cleaving peptide from Thosea asigna virus, Cre recombinase fused to the oestrogen receptor ligand binding domain (ER), bovine growth hormone poly(A), and a frt-flanked neomycin resistance cassette (suppl. Fig. 1A). The final construct was linearized with NotI and transfected by electroporation into C57BL/6 embryonic stem cells. Cells were grown on irradiated feeders with the aminoglycoside G418 in the media, and neomycin-resistant clones were screened for 5′ and 3′ homologous recombination by PCR. Two clones were selected for injection into albino C57BL/6 blastocysts to generate chimaeras, and the male pups with highest ratios of black-to-white coat colour from a single clone were selected to breed with homozygous *Gt(ROSA26)*$^{FLP1/FLP1}$ females (Jackson Laboratories; 009086) to excise the neomycin resistance cassette. Deletion of neomycin was confirmed by PCR. Mice were then crossed to C57BL/6 mice to remove the FLP1 allele and subsequently crossed to B6.129X1-*Gt(ROSA)26Sor*$^{tm1(EYFP)Cos}$/J (R26R-EYFP; Jackson Laboratories; 006148) for fate-mapping experiments.

All mice were generated on or backcrossed to the C57BL/6 background. Mice were maintained in the University of California San Francisco specific pathogen–free animal facility or UCSF Gnotobiotic Core Facility in accordance with the guidelines established by the Institutional Animal Care and Use Committee and Laboratory Animal Resource Center. SPF animals were housed in individually ventilated cage units that are changed every three weeks for maintenance cages and every other week for breeding cages; cage bottoms are covered with autoclaved bedding and nesting material for enrichment. Mice were fed irradiated food (PicoLab Mouse Diet 20, 5058M) and drink from autoclaved bottles or automatic watering system. All animals were manipulated using standard procedures including filtered air exchange stations, chlorine-based disinfection of gloves and work surfaces within manipulations with animals; personnel protection equipment (PPE) (disposable gowns, gloves, head caps, and shoe covers) is required to enter the facility. Experiments were carried out using age and gender matched groups.

METHOD DETAILS

Tissue dissociation—Mouse lungs were perfused through the right cardiac ventricle with cold PBS and underwent an initial mechanical dissociation using the m_lung_01_01 program on the gentleMACS dissociator (Miltenyi Biotec). Lung tissues were then digested

with 50 μg/ml Liberase TM (Roche) and 25 μg/ml DNase I (Roche) in pre-warmed RPMI-1640 for 30mins at 37°C. Further dissociation was performed using the m_lung_01_02 program on the gentleMACS dissociator. Single-cell suspensions were obtained after passing the homogenized samples through 70 μm cell strainers.

Mouse intestines were flushed with PBS and Peyer patches were removed when visible in older mice. Intestines were opened, thoroughly cleaned with PBS, and incubated for 20 min in 20 ml HBSS (Ca^{2+} and Mg^{2+} free) supplemented with 2% fetal calf serum (FCS), 10 mM HEPES (UCSF Cell Culture Facility) and 5 mM DTT. Supernatants were discarded and intestines were incubated for 15 min in 10 ml HBSS (Ca^{2+} and Mg^{2+} free) supplemented with 2% fetal calf serum (FCS), 10 mM HEPES (UCSF Cell Culture Facility) and 5 mM EDTA solution. This step was repeated twice using fresh solution. Next, intestines were incubated for 10 min in 20 ml HBSS (with Ca^{2+} and Mg^{2+}) supplemented with 3% FCS and 10 mM HEPES. After incubation, intestines were gently vortexed, cut into small pieces and incubated for 30 min in 5 ml HBSS (with Ca^{2+} and Mg^{2+}) supplemented with 3% FCS, 10 mM HEPES, 100 μg/ml Liberase TM (Roche) and 30 μg/ml DNase I (Roche). All the incubations were performed with gentle rocking at 37 °C.. After digest, intestines were mechanically dissociated in GentleMACS C tubes (Miltenyi Biotec) using program m_intestine_01, passed through a 100 μm filter, and washed. The resulting cell pellet was resuspended in 5 ml 40% Percoll (Sigma-Aldrich), underlaid with 5 ml 90% Percoll and centrifuged at 2000 r.p.m. for 20 min at 20 °C. The 40/90 interphase of the Percoll gradient was harvested, washed, and stained for flow cytometry.

Perigonadal visceral adipose tissue (VAT) was harvested and finely minced with scissors, followed by incubation for 40 min at 37° C in RPMI-1640 containing 100 μg/ml Liberase TM (Roche) and 50 μg/ml DNase I (Roche). The tissue was passed through 100 μm nylon filters, washed, and subjected to red blood cell lysis (PharmLyse; BD) before final suspension in FACS buffer.

Back skin was cut into small pieces and digested with 2 mg/ml Collagenase XI (Sigma C9407), 0.5 mg/ml Hyaluronidase (Sigma H3506), and 100 μg/ml DNase I (Roche) in pre-warmed RPMI-1640 for 90 min at 37°C with vigorous shaking. Afterwards, the tissues were further dissociated using the C program on the gentleMACS dissociator. Single-cell suspensions were obtained after passing the homogenized samples through 70 μcell strainers.

Flow cytometry—Fc block (anti-mouse CD16/32, 2.4G2) was purchased from BioXCell. Rat anti-mouse CD4 (RM4–5), rat anti-mouse CD11b (M1/70), rat anti-mouse CD19 (ID3), rat anti-mouse B220 (RB6–8C5), and rat anti-mouse CXCR5 (2G8) were purchased from BD Pharmingen; rat anti-mouse c-kit (2B8), rat anti-mouse CD3 (17A2), rat anti-mouse CD5 (53–7.3), rat anti-mouse CD127 (A7R34), rat anti-mouse NKp46 (29A1.4), rat anti-mouse α4β7 (DATK32), rat anti-human/mouse GATA-3 (TWAJ), rat anti-mouse MHC class II (M5/114.15.2), and mouse anti-mouse NK1.1 (PK136) antibodies were purchased from eBioscience; Armenian hamster anti-mouse CD11c (N418), Syrian hamster anti-mouse KLRG1 (2F1), rat anti-mouse CD45 (30-F11), rat anti-mouse Ter119 (TER-119), Armenian hamster anti-human/mouse/rat ICOS (C398.4A), rat anti-mouse CD25 (PC61), rat anti-

mouse Flt3 (A2F10), rat anti-mouse IL-17RB (9B10), rat anti-mouse CD90.2 (30-H12), rat anti-mouse F4/80 (BM8), rat anti-mouse CD115 (AFS98), PDGFRα (APA5), Sca-1 (D7), CD31 (390), EpCAM (G8.8), and Podoplanin (8.1.1) antibodies were purchased from Biolegend; and rat anti-mouse ST2 (DJ8) antibodies were purchased from MD Bioproducts. Lin- cells were defined as lacking CD3, CD4, CD5, CD8α, CD11b, CD11c, CD19, NK1.1, F4/80, Gr-1, FcεRIα, and Ter119. DAPI and Live/Dead (Invitrogen) was used for dead-cell exclusion for live and fixed samples, respectively. For intracellular staining of transcription factors, the FoxP3 Transcription Factor Staining Buffer Set (eBiosciences) was used according to manufacturer's instructions.

Samples were analyzed on a LSRFortessa X20 (BD Biosciences) with five lasers (355nm, 405nm, 488nm, 561nm, and 640nm). Samples were gated by FSC-A and SSC-A to exclude debris, FSC-H and FSC-W for single cells, and gated to exclude dead cells by DAPI (unfixed samples) or Live/Dead (fixed samples). Data analysis was performed using FlowJo (Treestar).

Parabiosis—Parabiosis surgery was performed following previously described procedures, which resulted in 40–60% mixing of circulating blood cells after 2 weeks (Villeda et al., 2014). Briefly, pairs of mice were joined by suturing mirror-image peritoneal openings, in addition to the elbow and knee joints, followed by stapling of the skin (9-mm autoclip, Clay Adams). Each mouse was then injected intraperitoneally (i.p.) with Baytril antibiotic and Buprenex analgesic, and over the first week of recovery after the surgery, each mouse received daily i.p. injections of 250cc normal saline. Several parameters, including pair weight and grooming behavior, were analyzed weekly after surgery to monitor overall health and recovery. We observed >70% survival at 5 weeks. Between 5 and 6 weeks after surgery, the pairs were euthanized and organs collected for processing and flow cytometric analysis.

Mouse treatments and infections—Mice were treated with tamoxifen dissolved at 20 mg/ml in corn oil (Sigma) for *Id2*^{CreERT2}, or at 40 mg/ml in EtOH supplemented with 1 volume of Cremophor EL (Sigma C5135) and 2 volumes of PBS for a final concentration of 10 mg/ml for *Arg1*$^{RFP\text{-}}$CreERT2 mice. Pregnant females were treated by oral gavage with 1 mg tamoxifen and 0.5 mg progesterone (Sigma P0130) twice daily on E16, 17 and 18. Day of embryonic development was estimated by taking the day of vaginal plug observation as E0.5. Because tamoxifen treatment during pregnancy interferes with normal delivery, pups were delivered by caesarean sections on E19.5 and neonates were fostered by lactating females. Neonatal pups were injected i.p. with 1.5 mg on P10 for *Id2*^{CreERT2}, or 400 μg on P10,11 and 12 for *Arg1*$^{RFP\text{-}CreERT2}$ mice. Adult mice were fed a tamoxifen chow (Envigo TD.130858) for 4 weeks. IL-7Rα blockade was performed by injecting 3 doses of 200 μg InVivoMAb anti-mouse IL-7Rα (A7R34, BioXCell) i.v. into timed pregnant females on E14.5, E16.5, and E18.5. For Nur77 stimulation, mice were injected i.p. with 1 μg rIL-33 (Biolegend) 16h prior to analysis. For infections with *N. brasiliensis*, mice were injected subcutaneously with 500 L3-stage larvae and analyzed at the indicated timepoints post-infection.

Cell sorting and scRNA-seq—ILC2s were sorted from homogenized mouse lung, skin, and small intestine as live (DAPI^{-}) CD45^{+}Lin^{-}

(CD3,CD4,CD5,CD8α,CD11b,CD11c,CD19,NK1.1, NKp46,Gr-1,F4/80,Ter-119,DX5)*Il5*$^{RFP+}$ cells. BM cells were sorted as live CD45^{+}Lin-Thy1^{+}Arg1^{YFP+} cells. Cells were sorted using a MoFlo XDP (Beckman Coulter) into ice-cold 0.5% BSA in PBS and processed on the same day through the Chromium Single Cell 3' v2 Library Kit (10X Genomics) per the manufacturer's protocol. Each channel was loaded with 5000–25000 cells from each tissue, yielding 400 single cells (neonatal small intestine), 3030 single cells (neonatal skin), 6348 single cells (neonatal lung), 7547 single cells (adult small intestine), 6115 single cells (adult skin), 11615 single cells (adult lung), and 4990 single cells (adult BM) for analysis. The cells were then partitioned into Gel Beads in Emulsion in the instrument, where cell lysis and barcoded reverse transcription of RNA occurred, followed by amplification, shearing, and 5' adaptor and sample index sequence ligation. Libraries were sequenced on an Illumina HiSeq 4000. Single Cell 3' libraries use standard Illumina sequencing primers for both sequencing and index reads. They were run using paired-end sequencing with single indexing where Read 1 is 26 cycles and Read 2 is 98 cycles.

Analysis of scRNA-seq data—FASTQ files were generated utilizing the Cell Ranger FASTQ ("cellranger mkfastq"; 10X Genomics) pipeline, through which resulting bcl files from sequencing are de-multiplexed using bcl2fastq (v. 2.17). The resultant paired-end FASTQ files were aligned utilizing the Cell Ranger Count ("cellranger count"; 10X Genomics) pipeline, though which FASTQ files are aligned to the mm10 reference transcriptome (Ensembl GRCm38 primary assembly) using STAR, an open source splicing-aware RNA-seq aligner, and then single-cell gene counts are generated. Outputs from the Cell Ranger Count pipeline were then run through the Cell Ranger Aggregator ("cellranger aggr") pipeline to combine data from neonatal and adult tissue ILC2 samples. Dimensionality reduction was also performed through the Cell Ranger pipeline, using principal components analysis (PCA) via a Python implementation of a modified version of the augmented implicitly restarted Lanczos bidiagonalization algorithm (IRLBA)(Baglama and Reichel, 2005). Data visualization of the PCA-reduced data was also performed through the Cell Ranger pipeline, using a modified version of the C++ reference implementation of *t*-SNE by Maaten, et al. (Maaten, 2014).

Accession Codes.: scRNA-seq data generated in this study are deposited in Gene Expression Omnibus (GEO) under accession code GSE126924 and GSE117568.

Quantitative RT–PCR—Single-cell epithelial suspensions were isolated, stained as described earlier and sorted using a MoFlo XDP (Beckman Coulter). RNA was isolated using the Micro Plus RNeasy kit (QIAGEN) and reverse transcribed using the SuperScript Vilo Master Mix (Life Technologies). The resulting cDNA was used as template for quantitative PCR (qPCR) with the Power SYBR Green reagent on a StepOnePlus cycler (Applied Biosystems). Transcripts were normalized to Rps17 (40S ribosomal protein S17) expression and relative expression shown as $2^{-\Delta Ct}$. Primer sequences (see also Key Resources Table): *Rps17*, 5'-CGCCATTATCCCCAGCAAG-3', 5'-TGTCGGGATCCACCTCAATG-3'; *Il33*, 5'-AAGACCAGGTGCTACTACGC-3', 5'-CTTCTTCCCATCCACACCGT-3'; *Tslp*, 5'-CCCTTCACTCCCCGACAAAA-3', 5'-

CCTGAGTACCGTCATTTCTCTCA-3'; *Il5*, 5'-CTCTGTTGACAAGCAATGAGACG-3', 5'-TCTTCAGTATGTCTAGCCCCTG-3'; *Il13*, 5'-CCTGGCTCTTGCTTGCCTT-3', 5'-GGTCTTGTGTGATGTTGCTCA-3'.

ILC2 culture and chemokine detection—$Lin^{-}CD45^{+}Thy1^{+}Red5^{+}$ ILC2s from lung and skin were FACS sorted and 2500 (lung) or 1000 (skin) cells per well were cultured in RPMI-1640 (Sigma) containing 10% FBS, 10 mM HEPES (Sigma), 100 μM non-essential amino acids (Sigma), 1 mM sodium pyruvate (Gibco), 100 μU/mL penicillin (Gibco), 100 μg/mL streptomycin (Gibco), 50 μM 2-mercaptoethanol (Gibco), 10 ng/ml rIL-7 (R&D Systems), 10 ng/ml rIL-2 (R&D Systems), and 10 ng/ml rIL-33 (BioLegend) in 96-well round bottom plates at 37 °C under 5% CO_2. After 3 days, supernatants were collected and the concentration of CXCL2 was measured by ELISA (ThermoFisher, EMCXCL2).

QUANTIFICATION AND STATISTICAL ANALYSIS

All experiments were performed using randomly assigned mice without investigator blinding. All data points and n values reflect biological replicates. No data were excluded. Where noted in the figures, statistical significance was calculated using two-tailed non-parametric Mann-Whitney *U* test or unpaired, two-tailed t-tests for the comparison between two experimental groups, or one-way ANOVA for multiple comparisons. Experimental groups included a minimum of three biological replicates. Intragroup variation was not assessed. All statistical analysis was performed using Prism 6 (GraphPad Software). Figures display means ± s.e.m. as indicated. No statistical methods were used to predetermine sample size.

Supplementary Material

Refer to Web version on PubMed Central for supplementary material.

ACKNOWLEDGMENTS

We thank Z. Wang, M. Ji and M. Consengco for technical expertise; members of the Locksley laboratory for discussions; M. Ansel and L. Lanier for manuscript comments; A.Y. Rudensky for providing the tdTomato-T2A-CreERT2 cassette; A.V. Molofsky for providing $Il7r^{-/-}$ mice; J. Turnbaugh and the UCSF Gnotobiotic Core Facility for germfree mice; support from DRC NIH P30 DK63720 for gene targeting; A.B Molofsky and S. van Dyken for assistance with cell isolation; and D. Vaka for assistance with scRNA-seq data analysis. This work was supported by the National Institutes of Health (R01AI026918 and R01HL128903 to R.M.L., F30AI122702 and T32GM007618 to J.L.), Howard Hughes Medical Institute, the Australian NHMRC (APP1143020) and the Sandler Asthma Basic Research Center at the UCSF. C.S. is supported by fellowships from the Swiss National Science Foundation (P2EZP3_162266; P300PA_171591). R.R.R.-G. is supported by grants from the Dermatology Foundation, A.P. Giannini Foundation, and the Robert Wood Johnson Foundation.

REFERENCES

Baglama J, and Reichel L (2005). Augmented Implicitly Restarted Lanczos Bidiagonalization Methods. SIAM J. Sci. Comput 27, 19–42.

Bando JK, Nussbaum JC, Liang H-E, and Locksley RM (2013). Type 2 innate lymphoid cells constitutively express arginase-I in the naïve and inflamed lung. J Leukoc Biol 94, 877–884. [PubMed: 23924659]

Bando JK, Liang H-E, and Locksley RM (2015). Identification and distribution of developing innate lymphoid cells in the fetal mouse intestine. Nat Immunol 16, 153–160. [PubMed: 25501629]

Beaudin AE, and Forsberg EC (2016). To B1a or not to B1a: do hematopoietic stem cells contribute to tissue-resident immune cells? Blood 128, 2765–2769. [PubMed: 27799163]

Beaudin AE, Boyer SW, Perez-Cunningham J, Hernandez GE, Derderian SC, Jujjavarapu C, Aaserude E, MacKenzie T, and Forsberg EC (2016). A Transient Developmental Hematopoietic Stem Cell Gives Rise to Innate-like B and T Cells. Cell Stem Cell 19, 768–783. [PubMed: 27666010]

Boos MD, Yokota Y, Eberl G, and Kee BL (2007). Mature natural killer cell and lymphoid tissue–inducing cell development requires Id2-mediated suppression of E protein activity. J Exp Med 204, 1119–1130. [PubMed: 17452521]

Camberis M, Gros GL, and Urban J Animal Model of Nippostrongylus brasiliensis and Heligmosomoides polygyrus. Current Protocols in Immunology 55, 19.12.1–19.12.27.

Carding SR, and Egan PJ (2002). γδ T cells: functional plasticity and heterogeneity. Nature Reviews Immunology 2, 336–345.

Constantinides MG, McDonald BD, Verhoef PA, and Bendelac A (2014). A committed precursor to innate lymphoid cells. Nature 508, 397–401. [PubMed: 24509713]

Dahlgren M, Jones S, Cuativo K, Dubinin A, Farhat S, Ortiz-Carpena J, Yu K, Lee K, Wang C, Molofsky A, et al. (2019). Adventitial stromal cells define group 2 innate lymphoid cell tissue niches. Immunity 50, 707–722. [PubMed: 30824323]

Ebbo M, Crinier A, Vély F, and Vivier E (2017). Innate lymphoid cells: major players in inflammatory diseases. Nature Reviews Immunology 17, 665–678.

Eberl G, Marmon S, Sunshine M-J, Rennert PD, Choi Y, and Littman DR (2004). An essential function for the nuclear receptor RORγt in the generation of fetal lymphoid tissue inducer cells. Nature Immunology 5, 64–73. [PubMed: 14691482]

Fan X, and Rudensky AY (2016). Hallmarks of Tissue-Resident Lymphocytes. Cell 164, 1198–1211. [PubMed: 26967286]

van Furth R, and Cohn ZA (1968). The origin and kinetics of mononuclear phagocytes. J Exp Med 128, 415–435. [PubMed: 5666958]

Gasteiger G, Fan X, Dikiy S, Lee SY, and Rudensky AY (2015). Tissue residency of innate lymphoid cells in lymphoid and nonlymphoid organs. Science 350, 981–985. [PubMed: 26472762]

Gentek R, Ghigo C, Hoeffel G, Bulle MJ, Msallam R, Gautier G, Launay P, Chen J, Ginhoux F, and Bajénoff M (2018). Hemogenic Endothelial Fate Mapping Reveals Dual Developmental Origin of Mast Cells. Immunity 19, 1160–1171.e5.

Ghaedi M, Steer CA, Martinez-Gonzalez I, Halim TYF, Abraham N, and Takei F (2016). Common-Lymphoid-Progenitor-Independent Pathways of Innate and T Lymphocyte Development. Cell Reports 15, 471–480. [PubMed: 27068476]

Gibbings SL, Goyal R, Desch AN, Leach SM, Prabagar M, Atif SM, Bratton DL, Janssen W, and Jakubzick CV (2015). Transcriptome analysis highlights the conserved difference between embryonic and postnatal-derived alveolar macrophages. Blood 126, 1357–1366. [PubMed: 26232173]

Ginhoux F, and Guilliams M (2016). Tissue-Resident Macrophage Ontogeny and Homeostasis. Immunity 44, 439–449. [PubMed: 26982352]

Gollwitzer ES, and Marsland BJ (2015). Impact of Early-Life Exposures on Immune Maturation and Susceptibility to Disease. Trends in Immunology 36, 684–696. [PubMed: 26497259]

Hoeffel G, and Ginhoux F (2015). Ontogeny of Tissue-Resident Macrophages. Front Immunol 6, 486. [PubMed: 26441990]

Hoyler T, Klose CSN, Souabni A, Turqueti-Neves A, Pfeifer D, Rawlins EL, Voehringer D, Busslinger M, and Diefenbach A (2012). The Transcription Factor GATA-3 Controls Cell Fate and Maintenance of Type 2 Innate Lymphoid Cells. Immunity 37, 634–648. [PubMed: 23063333]

Huang Y, Mao K, Chen X, Sun M-A, Kawabe T, Li W, Usher N, Zhu J, Urban JF, Paul WE, et al. (2018). S1P-dependent interorgan trafficking of group 2 innate lymphoid cells supports host defense. Science 359, 114–119. [PubMed: 29302015]

Ishizuka IE, Chea S, Gudjonson H, Constantinides MG, Dinner AR, Bendelac A, and Golub R (2016). Single-cell analysis defines the divergence between the innate lymphoid cell lineage and lymphoid tissue-inducer cell lineage. Nat. Immunol 17, 269–276. [PubMed: 26779601]

Kleer I.M. de, Kool M, Bruijn M.J.W. de, Willart M, Moorleghem J van, Schuijs MJ, Plantinga M, Beyaert R, Hams E, Fallon PG, et al. (2016). Perinatal Activation of the Interleukin-33 Pathway Promotes Type 2 Immunity in the Developing Lung. Immunity 45, 1285–1298. [PubMed: 27939673]

Klose CSN, and Artis D (2016). Innate lymphoid cells as regulators of immunity, inflammation and tissue homeostasis. Nat. Immunol 17, 765–774. [PubMed: 27328006]

Klose CSN, Flach M, Möhle L, Rogell L, Hoyler T, Ebert K, Fabiunke C, Pfeifer D, Sexl V, Fonseca-Pereira D, et al. (2014). Differentiation of Type 1 ILCs from a Common Progenitor to All Helper-like Innate Lymphoid Cell Lineages. Cell 157, 340–356. [PubMed: 24725403]

Koga S, Hozumi K, Hirano K-I, Yazawa M, Terooatea T, Minoda A, Nagasawa T, Koyasu S, and Moro K (2018). Peripheral PDGFRα+gp38+ mesenchymal cells support the differentiation of fetal liver-derived ILC2. J Exp Med 215, 1609–1626. [PubMed: 29728440]

Lambrecht BN, and Hammad H (2017). The immunology of the allergy epidemic and the hygiene hypothesis. Nat. Immunol 18, 1076–1083. [PubMed: 28926539]

Lavin Y, Winter D, Blecher-Gonen R, David E, Keren-Shaul H, Merad M, Jung S, and Amit I (2014). Tissue-resident macrophage enhancer landscapes are shaped by the local microenvironment. Cell 159, 1312–1326. [PubMed: 25480296]

Liang H-E, Reinhardt RL, Bando JK, Sullivan BM, Ho I-C, and Locksley RM (2012). Divergent expression patterns of IL-4 and IL-13 define unique functions in allergic immunity. Nat Immunol 13, 58–66.

Maaten L. van der (2014). Accelerating t-SNE using Tree-Based Algorithms. Journal of Machine Learning Research 15, 3221–3245.

Mass E, Ballesteros I, Farlik M, Halbritter F, Günther P, Crozet L, Jacome-Galarza CE, Händler K, Klughammer J, Kobayashi Y, et al. (2016). Specification of tissue-resident macrophages during organogenesis. Science 353, aaf4238. [PubMed: 27492475]

Maxwell MA, and Muscat GEO (2006). The NR4A subgroup: immediate early response genes with pleiotropic physiological roles. Nucl Recept Signal 4, e002. [PubMed: 16604165]

McGrath KE, Frame JM, and Palis J (2015). Early hematopoiesis and macrophage development. Semin Immunol 27, 379–387. [PubMed: 27021646]

Montecino-Rodriguez E, Fice M, Casero D, Berent-Maoz B, Barber CL, and Dorshkind K (2016). Distinct Genetic Networks Orchestrate the Emergence of Specific Waves of Fetal and Adult B-1 and B-2 Development. Immunity 45, 527–539. [PubMed: 27566938]

Monticelli LA, Buck MD, Flamar A-L, Saenz SA, Tait Wojno ED, Yudanin NA, Osborne LC, Hepworth MR, Tran SV, Rodewald H-R, et al. (2016). Arginase 1 is an innate lymphoid-cell-intrinsic metabolic checkpoint controlling type 2 inflammation. Nat. Immunol 17, 656–665. [PubMed: 27043409]

Moro K, Yamada T, Tanabe M, Takeuchi T, Ikawa T, Kawamoto H, Furusawa J-I, Ohtani M, Fujii H, and Koyasu S (2010). Innate production of T(H)2 cytokines by adipose tissue-associated c-Kit(+)Sca-1(+) lymphoid cells. Nature 463, 540–544. [PubMed: 20023630]

Moro K, Kabata H, Tanabe M, Koga S, Takeno N, Mochizuki M, Fukunaga K, Asano K, Betsuyaku T, and Koyasu S (2016). Interferon and IL-27 antagonize the function of group 2 innate lymphoid cells and type 2 innate immune responses. Nat. Immunol 17, 76–86. [PubMed: 26595888]

Neill DR, Wong SH, Bellosi A, Flynn RJ, Daly M, Langford TKA, Bucks C, Kane CM, Fallon PG, Pannell R, et al. (2010). Nuocytes represent a new innate effector leukocyte that mediates type-2 immunity. Nature 464, 1367–1370. [PubMed: 20200518]

Nussbaum JC, Van Dyken SJ, von Moltke J, Cheng LE, Mohapatra A, Molofsky AB, Thornton EE, Krummel MF, Chawla A, Liang H-E, et al. (2013). Type 2 innate lymphoid cells control eosinophil homeostasis. Nature 502, 245–248. [PubMed: 24037376]

Olin A, Henckel E, Chen Y, Lakshmikanth T, Pou C, Mikes J, Gustafsson A, Bernhardsson AK, Zhang C, Bohlin K, et al. (2018). Stereotypic Immune System Development in Newborn Children. Cell 174, 1277–1292.e14. [PubMed: 30142345]

Pawankar R, Canonica G, Holgate S, and Lockey R (2011). Introduction and Executive Summary: Establishing the need to treat allergic diseases as a global public health issue In WAO White Book on Allergy, (United Kingdom).

Price AE, Liang H-E, Sullivan BM, Reinhardt RL, Eisley CJ, Erle DJ, and Locksley RM (2010). Systemically dispersed innate IL-13-expressing cells in type 2 immunity. Proceedings of the National Academy of Sciences of the United States of America 107, 11489–11494. [PubMed: 20534524]

Rawlins EL, Clark CP, Xue Y, and Hogan BLM (2009). The Id2+ distal tip lung epithelium contains individual multipotent embryonic progenitor cells. Development 136, 3741–3745. [PubMed: 19855016]

Reese TA, Liang H-E, Tager AM, Luster AD, Van Rooijen N, Voehringer D, and Locksley RM (2007). Chitin induces accumulation in tissue of innate immune cells associated with allergy. Nature 447, 92–96. [PubMed: 17450126]

Ricardo-Gonzalez RR, Van Dyken SJ, Schneider C, Lee J, Nussbaum JC, Liang H-E, Vaka D, Eckalbar WL, Molofsky AB, Erle DJ, et al. (2018). Tissue signals imprint ILC2 identity with anticipatory function. Nat. Immunol 19, 1093–1099. [PubMed: 30201992]

Robinette ML, Fuchs A, Cortez VS, Lee JS, Wang Y, Durum SK, Gilfillan S, Colonna M, and Immunological Genome Consortium (2015). Transcriptional programs define molecular characteristics of innate lymphoid cell classes and subsets. Nat. Immunol 16, 306–317. [PubMed: 25621825]

Saluzzo S, Gorki A-D, Rana BMJ, Martins R, Scanlon S, Starkl P, Lakovits K, Hladik A, Korosec A, Sharif O, et al. (2017). First-Breath-Induced Type 2 Pathways Shape the Lung Immune Environment. Cell Reports 18, 1893–1905. [PubMed: 28228256]

Sawa S, Cherrier M, Lochner M, Satoh-Takayama N, Fehling HJ, Langa F, Di Santo JP, and Eberl G (2010). Lineage relationship analysis of RORgammat+ innate lymphoid cells. Science 330, 665–669. [PubMed: 20929731]

Sawai CM, Babovic S, Upadhaya S, Knapp DJHF, Lavin Y, Lau CM, Goloborodko A, Feng J, Fujisaki J, Ding L, et al. (2016). Hematopoietic Stem Cells Are the Major Source of Multilineage Hematopoiesis in Adult Animals. Immunity 45, 597–609. [PubMed: 27590115]

Schneider C, O'Leary CE, Moltke J. von, Liang H-E, Ang QY, Turnbaugh PJ, Radhakrishnan S, Pellizzon M, Ma A, and Locksley RM (2018). A Metabolite-Triggered Tuft Cell-ILC2 Circuit Drives Small Intestinal Remodeling. Cell 174, 271–284e14. [PubMed: 29887373]

Shaw TN, Houston SA, Wemyss K, Bridgeman HM, Barbera TA, Zangerle-Murray T, Strangward P, Ridley AJL, Wang P, Tamoutounour S, et al. (2018). Tissue-resident macrophages in the intestine are long lived and defined by Tim-4 and CD4 expression. J Exp Med 215, 1507–1518. [PubMed: 29789388]

Smith NL, Patel RK, Reynaldi A, Grenier JK, Wang J, Watson NB, Nzingha K, Yee Mon KJ, Peng SA, Grimson A, et al. (2018). Developmental Origin Governs CD8+ T Cell Fate Decisions during Infection. Cell 174, 117–130.e14. [PubMed: 29909981]

Steer CA, Martinez-Gonzalez I, Ghaedi M, Allinger P, Mathä L, and Takei F (2017). Group 2 innate lymphoid cell activation in the neonatal lung drives type 2 immunity and allergen sensitization. Journal of Allergy and Clinical Immunology 140, 593–595.e3. [PubMed: 28216436]

Tamoutounour S, Guilliams M, Montanana Sanchis F, Liu H, Terhorst D, Malosse C, Pollet E, Ardouin L, Luche H, Sanchez C, et al. (2013). Origins and functional specialization of macrophages and of conventional and monocyte-derived dendritic cells in mouse skin. Immunity 39, 925–938. [PubMed: 24184057]

Villeda SA, Plambeck KE, Middeldorp J, Castellano JM, Mosher KI, Luo J, Smith LK, Bieri G, Lin K, Berdnik D, et al. (2014). Young blood reverses age-related impairments in cognitive function and synaptic plasticity in mice. Nature Medicine 20, 659–663.

Yang S, Fujikado N, Kolodin D, Benoist C, and Mathis D (2015). Regulatory T cells generated early in life play a distinct role in maintaining self-tolerance. Science 348, 589–594. [PubMed: 25791085]

Yokota Y, Mansouri A, Mori S, Sugawara S, Adachi S, Nishikawa S-I, and Gruss P (1999). Development of peripheral lymphoid organs and natural killer cells depends on the helix–loop–helix inhibitor Id2. Nature 397, 702–706. [PubMed: 10067894]

Zikherman J, Parameswaran R, and Weiss A (2012). Endogenous antigen tunes the responsiveness of naive B cells but not T cells. Nature 489, 160–164. [PubMed: 22902503]

Highlights

- Adult ILC2 pools are comprised of cells with fetal, postnatal, and adult origin
- Adult ILC2 pool dilution by *de novo* generated ILC2s is dynamic but varies by tissue
- Neonatal ILC2s activate effector repertoires and acquire tissue-specific signatures
- Worm infection drives expansion of pre-existing ILC2 pools not *de novo* generation

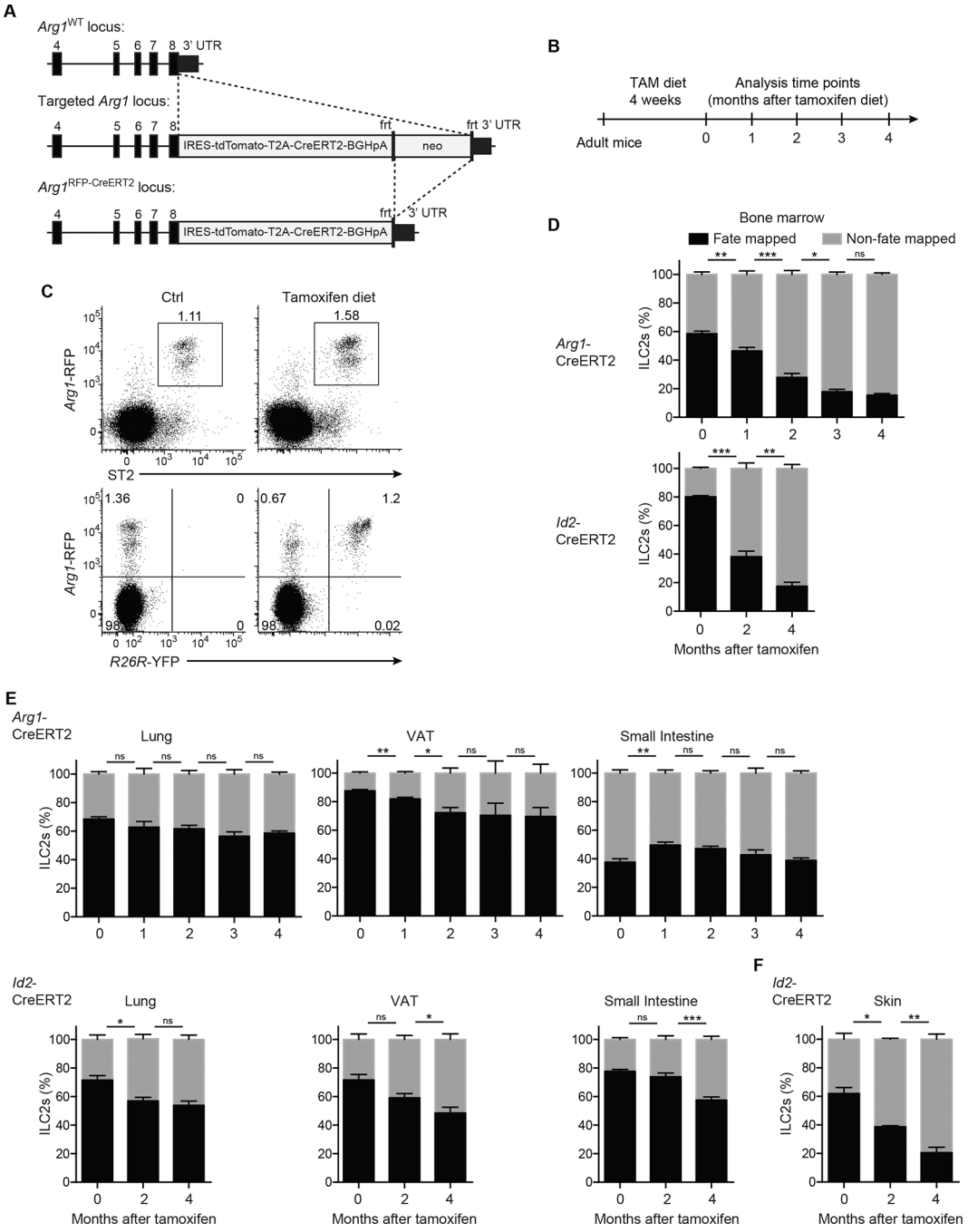

Figure 1. Tissue ILC2s are replaced by *de novo* generated ILC2s at a low rate.

(A) Gene-targeting strategy for the *Arg1*$^{\text{RFP-CreERT2}}$ mouse. (B-F) Adult *Arg1*$^{\text{RFP-CreERT2}}$*R26R*$^{\text{YFP}}$ and *Id2*$^{\text{CreERT2}}$*R26R*$^{\text{RFP}}$ mice were treated with tamoxifen chow according to schedule (B). (C) Expression of *Arg1*-RFP and ST2 (top) or R26R-YFP (bottom) by cells gated on CD45^{+} cells isolated from the lung of *Arg1*$^{\text{RFP-CreERT2}}$*R26R*$^{\text{YFP}}$ mice after 4 weeks of tamoxifen diet. (D-F) Percentages of fate-mapped ILC2s in BM (D), lung, visceral adipose tissue (VAT), and small intestine lamina propria (E), and skin (F) analyzed at indicated time points. ILC2s gated as Lin^{-} α4β7^{+}IL-7R^{+}Thy1^{+}CD25^{+} (BM),

$Lin^{-}Thy1^{+}ST2^{+}$ (lung and VAT), $Lin^{-}IL17RB^{+}KLRG1^{+}$ (small intestine), or $Lin^{-}Thy1^{+}ICOS^{+}$ (skin). Data from one experiment representative of at least three independent experiments (C) or pooled from multiple independent experiments and displayed as mean ± SEM of 4–7 individual mice per group and time point (D-F). See also Figure S1.

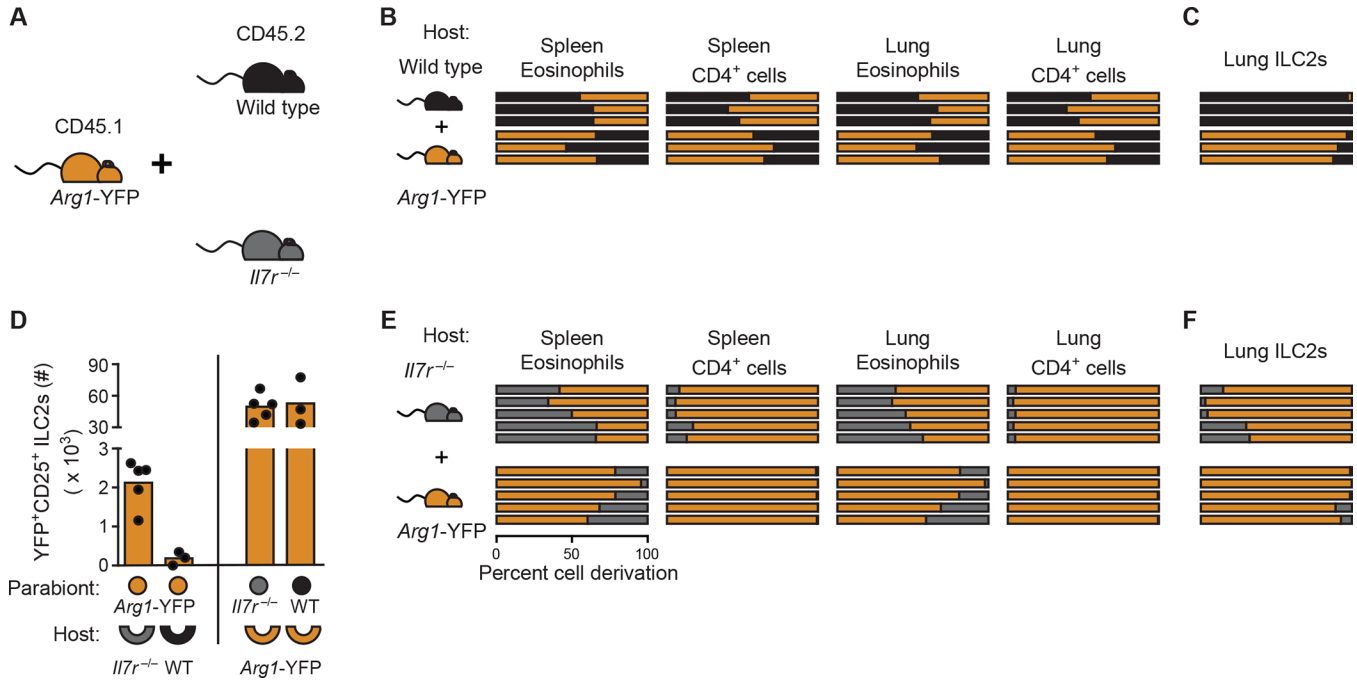

Figure 2. Low progenitor recirculation frequency and restricted niche availability cause minimal replacement of adult tissue ILC2s.

(A) Schematic of CD45.1 *Arg1*-YFP reporter mice (yellow) parabiosis with either WT (black) or *Il7r*$^{-/-}$ (gray) mice. (B and C) Percent derivation of (B) eosinophils and CD4^{+} T cells from spleen and lung and (C) ILC2s from the lung; each bar represents a single mouse from the WT:*Arg1*-YFP pair. (D) Numbers of lung Arg1^{+} CD25^{+} ILC2s; each dot represents one host mouse. Percent derivation of (E) eosinophils and CD4^{+} T cells from the spleen and lung and (F) ILC2s from the lung; each bar represents a single mouse from the *Il7r*$^{-/-}$:*Arg1*-YFP pair. Data are from one surgery cohort and representative of three independent surgery cohorts. See also Figure S2.

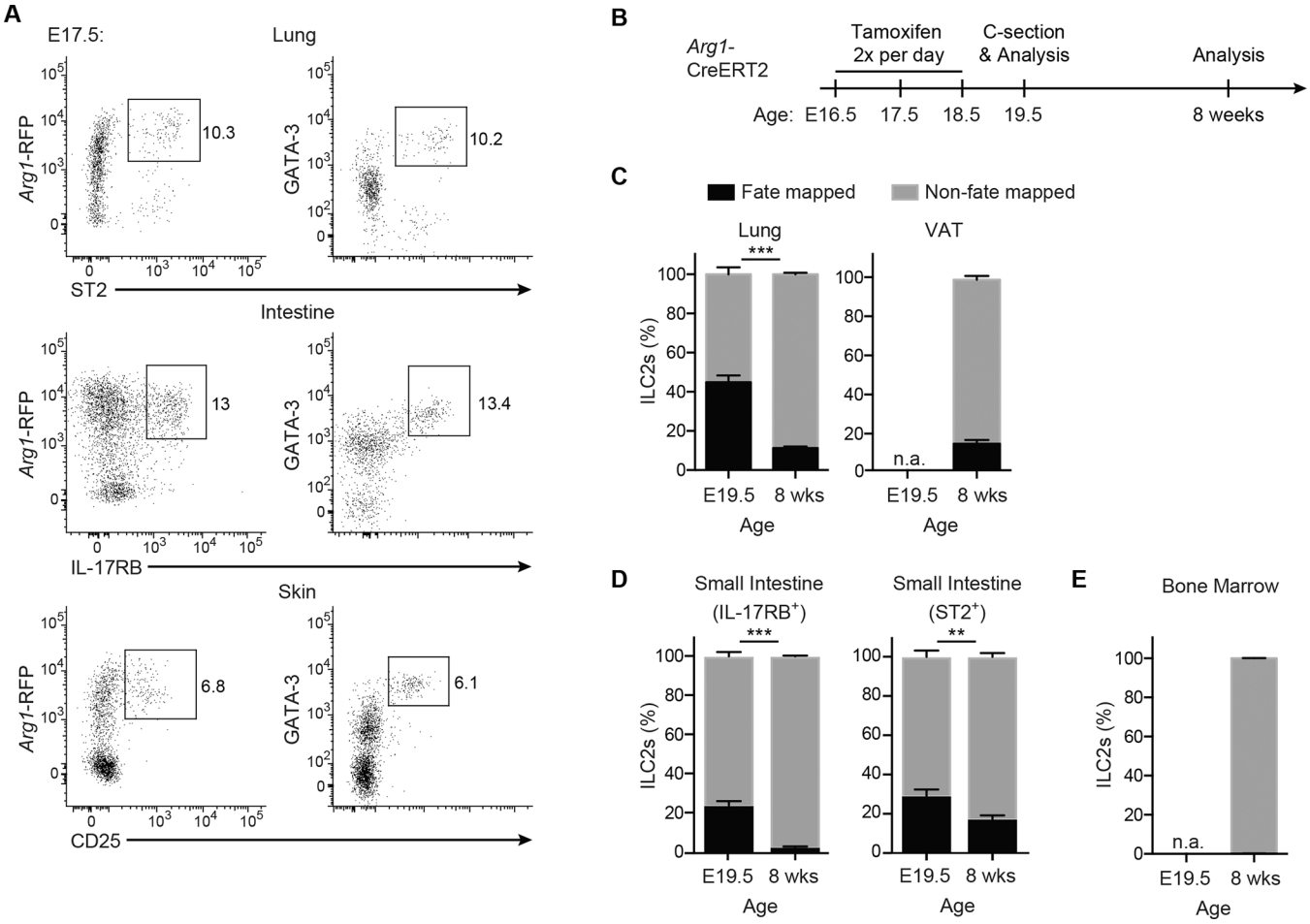

Figure 3. Prenatal ILC2 precursors seed tissues during fetal development and contribute to the adult ILC2 tissue pool.

(A) Expression of *Arg1* (left) or GATA-3 (right), and ST2, IL-17RB, or CD25 by cells gated on Lin$^-$ CD45$^+$ cells isolated from the lung, small intestine, and skin of *Arg1*$^{\text{RFP-CreERT2}}$ reporter mice on embryonic day 17.5 (E17.5). (B-E) Pregnant *Arg1*$^{\text{RFP-CreERT2}}$*R26R*$^{\text{YFP}}$ mice treated with tamoxifen according to schedule in (B). (C-E) Percentages of fate-mapped ILC2s in lung and visceral adipose tissue (C), small intestine lamina propria (D), and BM (E) analyzed in E19.5 and 2-month-old mice. ILC2s gated as Lin$^-$Thy1$^+$ST2$^+$ (lung and VAT), Lin$^-$IL-17RB$^+$KLRG1$^+$ or Lin$^-$ST2$^+$KLRG1$^+$ as indicated for the small intestine, or Lin$^-$IL-7Rα$^+$Thy1$^+$CD25$^+$ (BM); n.a., not assessed. Data from one experiment representative of at least three independent experiments (A) or pooled from multiple independent experiments and displayed as mean ± SEM of 6–8 individual mice per group and time point (C-E). See also Figure S3.

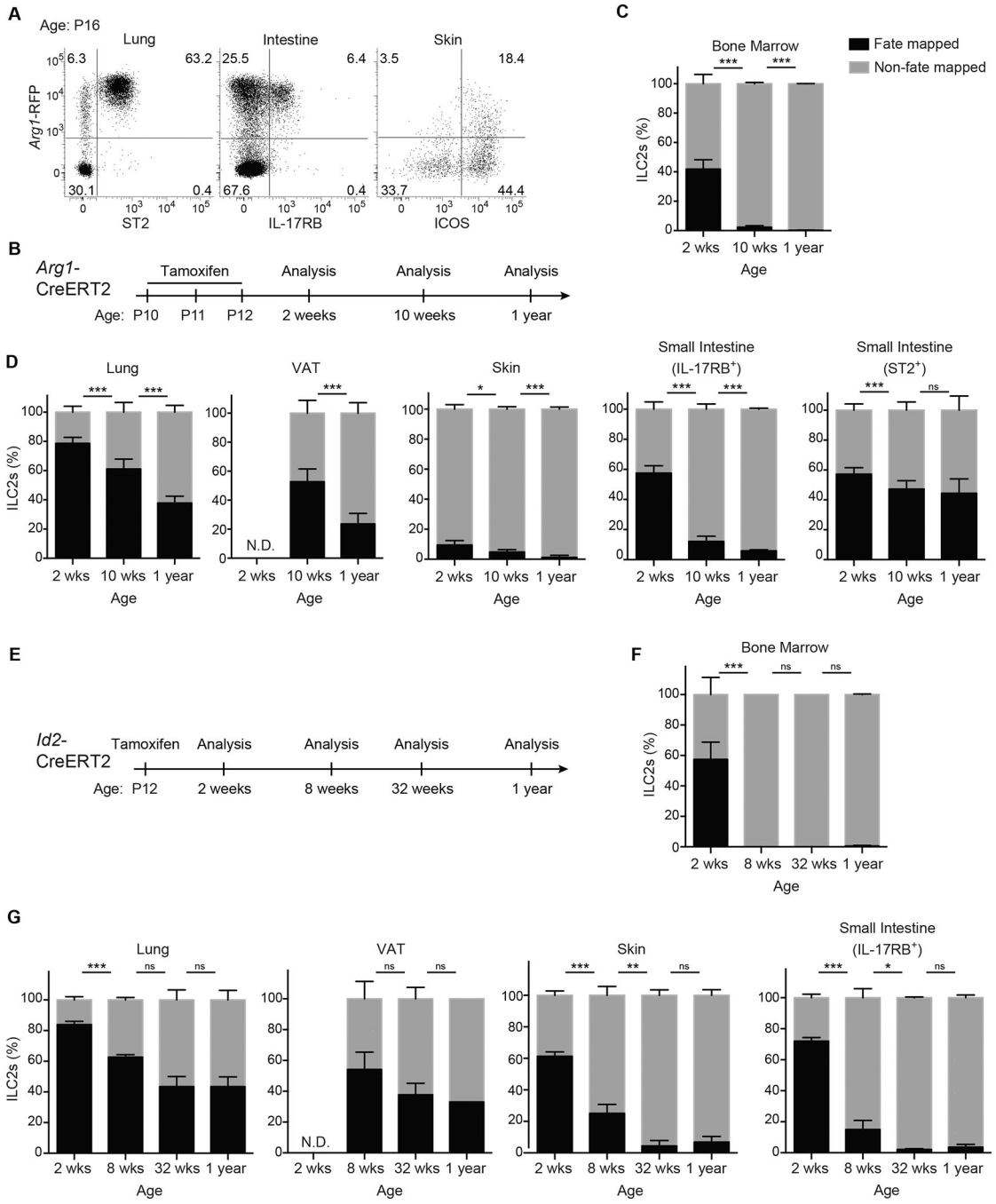

Figure 4. Neonatal ILC2s contribute to the majority of the ILC2 pool in adult tissues.

(A) Expression of *Arg1*-RFP, and ST2, IL-17RB, or ICOS by cells gated on Lin$^-$ CD45$^+$ cells isolated from lung, small intestine, and skin of *Arg1*$^{\text{RFP-CreERT2}}$ reporter mice on postnatal day 16 (P16). (B-F) Neonatal *Arg1*$^{\text{RFP-CreERT2}}$*R26R*$^{\text{YFP}}$ and *Id2*$^{\text{CreERT2}}$*R26R*$^{\text{RFP}}$ mice treated with tamoxifen according to schedule in (B,E). Percentages of fate mapped ILC2s in BM (C), and lung, visceral adipose tissue (VAT), skin, and small intestine lamina propria (D) of *Arg1*$^{\text{RFP-CreERT2}}$*R26R*$^{\text{YFP}}$ mice. Percentages of fate mapped ILC2s in the BM (F), and lung, visceral adipose tissue, skin, and small intestine lamina propria (G) of

Id2^{CreERT2}*R26R*^{RFP} mice. ILC2s gated as in Fig. 3. Data from one experiment representative of at least three independent experiments (A) or pooled from multiple independent experiments and displayed as mean ± SEM of 5–9 individual mice per group and time point (C-G).

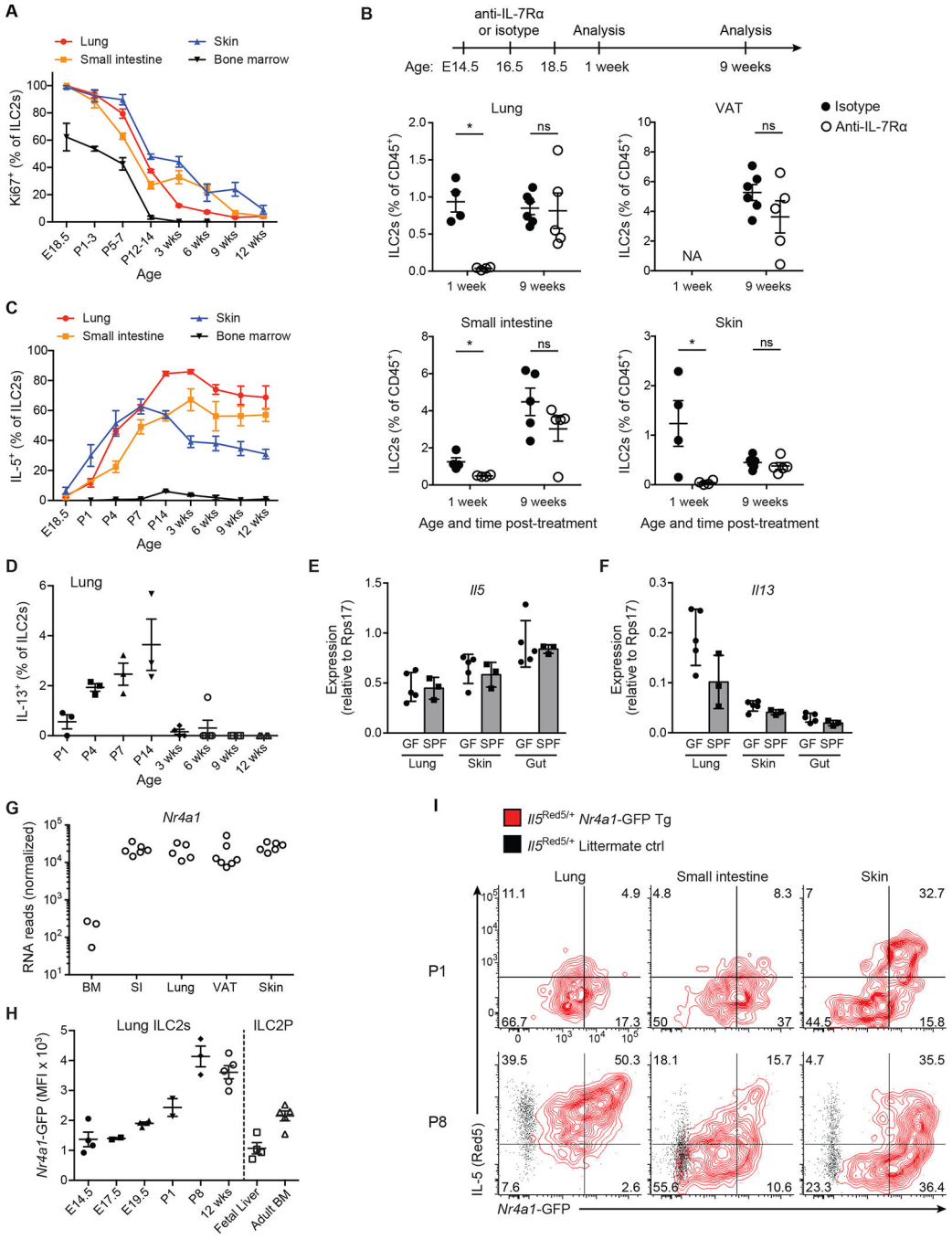

Figure 5. Vigorous perinatal ILC2 activation and proliferation is associated with Nur77 expression.

(A) Percentages of Ki-67^{+} ILC2s in the lung, small intestine lamina propria, skin, and BM analyzed on the indicated embryonic (E) and postnatal (P) time points. (B) Pregnant mice treated with anti-IL-7Rα blocking antibody (A7R34) on E14.5, E16.5, and E18.5, and percentages of ILC2s among CD45^{+} cells analyzed in lung, visceral adipose tissue (VAT), small intestine, and skin in 1 and 9 wks old mice. (C) Percentages of IL-5-reporter^{+} ILC2s in lung, small intestine, skin, and BM of *Il5*^{Red5} mice analyzed on the indicated time points. (D) Percentages of IL-13-reporter^{+} ILC2s in lung of *Il13*^{Sm13} mice. (E,F) Expression of *Il5*

(E) and *Il13* (F) by ILC2s sorted from individual SPF or germ-free neonatal mice analyzed by qPCR. (G) RNA-seq analysis of Nur77 (*Nr4a1*) transcripts (fragments per kilobase of exon per million mapped reads [FPKM]; averaged) among sorted IL-5 reporter^{+} ILC2s from indicated organs of adult mice (Ricardo-Gonzalez et al., 2018). BM, bone marrow. (H,I) *Nr4a1* expression measured by flow cytometry in ILC2s of *Nr4a1*-GFP reporter mice on indicated time points. (H) MFI of *Nr4a1*-GFP in ILC2s and ILC2Ps from lung, fetal liver and BM is displayed. (I) Expression of *Nr4a1*-GFP and IL-5-reporter by ILC2s from lung, small intestine, and skin of *Il5*$^{Red5/+}$*Nr4a1*-GFP mice on postnatal (P) day 1 and 8. ILC2s gated as Lin-Thy1^{+}ST2^{+} (lung and VAT), Lin^{-}IL-17RB^{+}KLRG1^{+} (adult small intestine), Lin^{-}IL-17RB^{+} (neonatal small intestine), Lin^{-}Thy1^{+}CD25^{+}ICOS^{+} (skin), or Lin^{-}IL-7Rα^{+} Thy1^{+}CD25^{+} (BM). Data pooled from multiple independent experiments (A,C,D,G,H) or from one experiment representative of at least two independent experiments (B,I) are shown. (A,C; mean and SEM, n = 3–10). See also Figure S4.

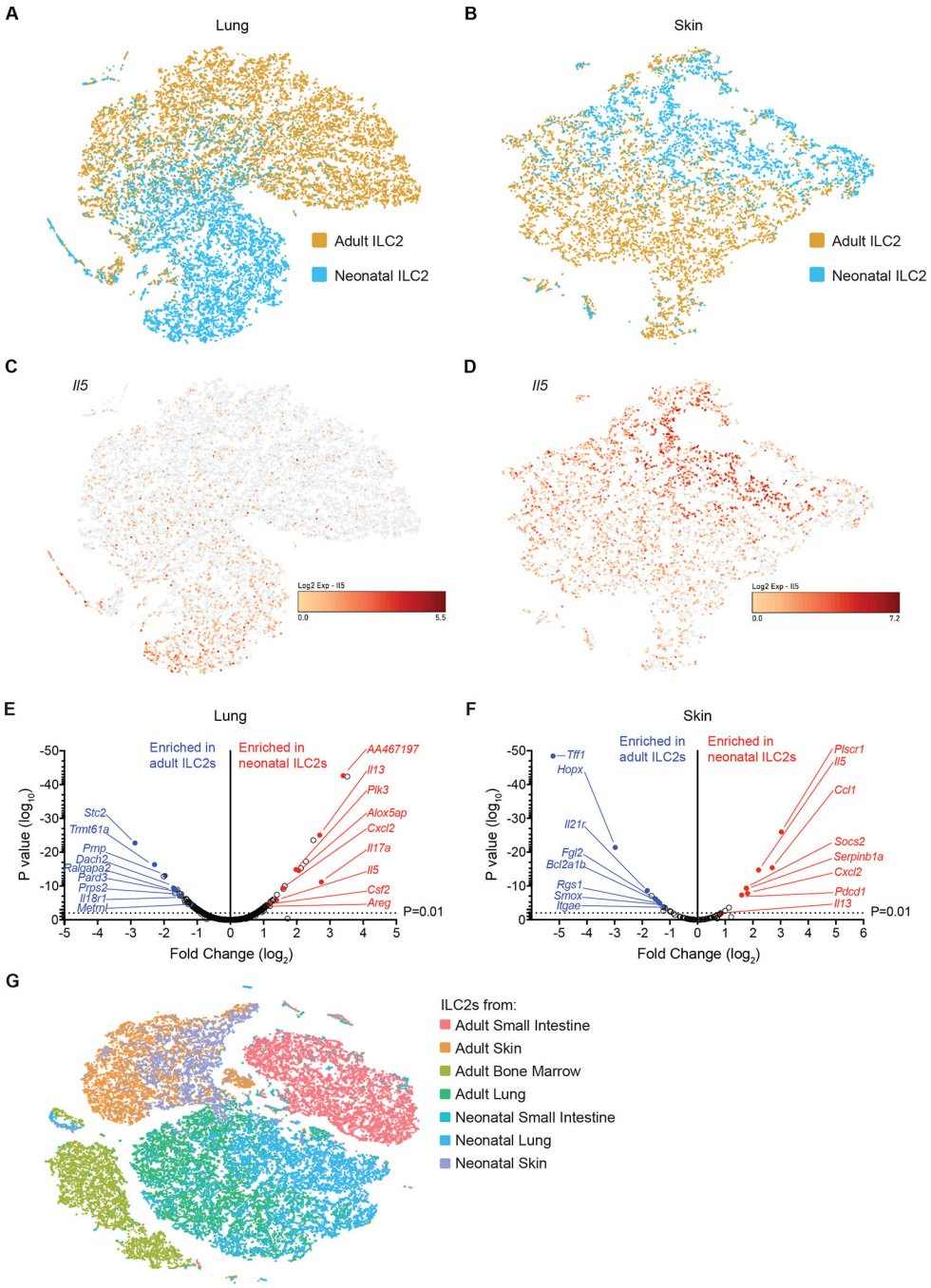

Figure 6. Tissue-specific heterogeneity of ILC2s is established in the early postnatal wave.

(A-G) IL-5-reporter^{+} ILC2s sorted from lung, skin and small intestine of neonatal (p14) *Il5*$^{Red5/+}$ mice and analyzed by scRNA-seq together with ILC2s from adult tissues processed on the same day (Ricardo-Gonzalez et al., 2018). (A,B) t-SNE visualization of adult and neonatal scRNA-seq datasets from lung (A) and skin (B). (C,D) Relative single-cell *Il5* expression in lung (C) and skin (D) ILC2s. (E,F) Volcano plots of differential gene expression between neonatal and adult ILC2s. Genes with an average expression of less than 1 transcript per 10 cells were excluded from analysis. (G) t-SNE visualization of adult (BM,

lung, adipose, skin, small intestine) and neonatal (lung, skin, small intestine) scRNA-seq datasets of sorted ILC2s. See also Figures S5 and S6.

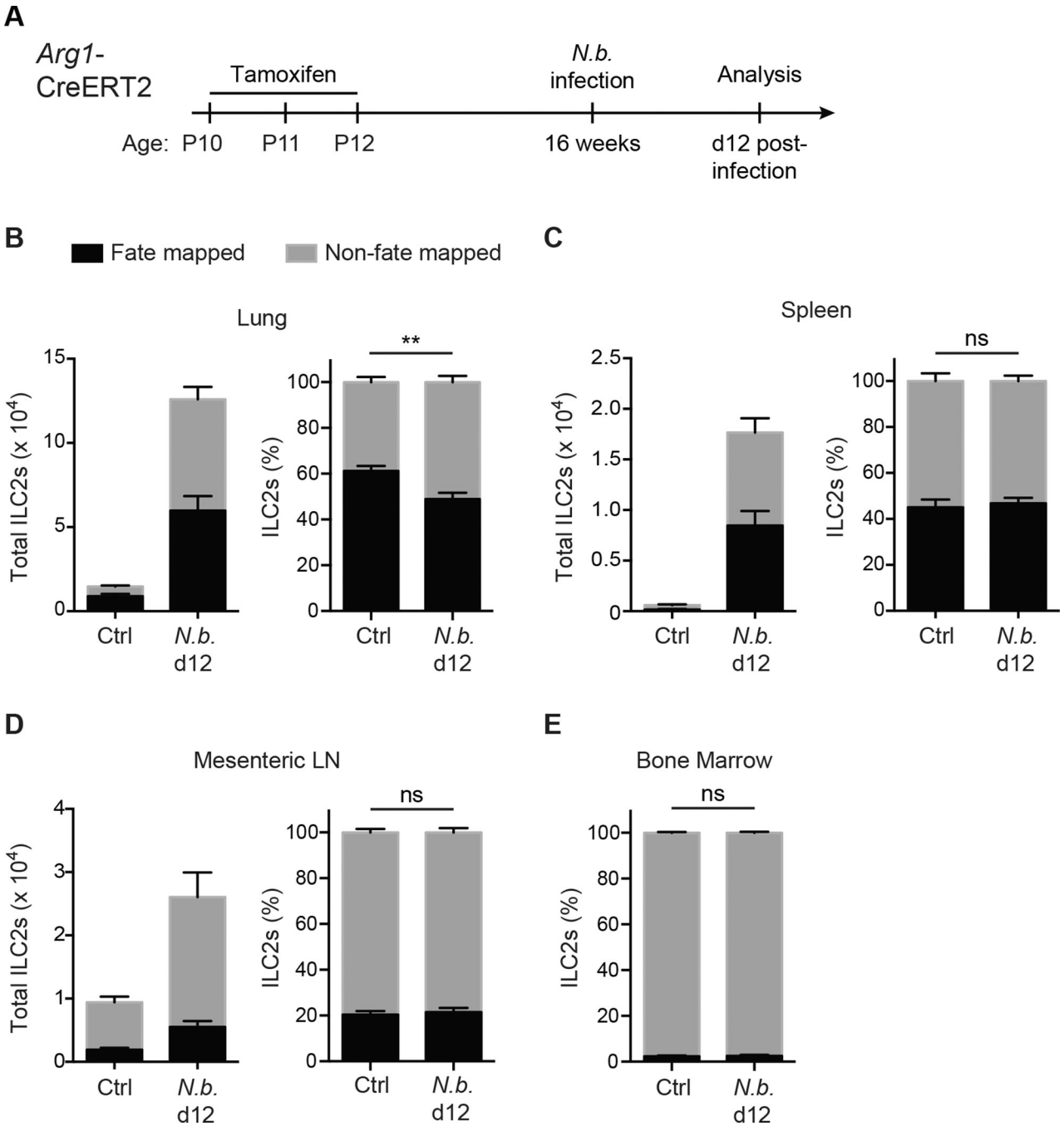

Figure 7. De novo generated ILC2s do not contribute to ILC2 expansion accompanying migratory helminth infection.

(A-E) *Arg1*$^{\text{RFP-CreERT2}}$*R26R*$^{\text{YFP}}$ mice tamoxifen-treated on p10, 11 and 12 and infected with *N. brasiliensis* (*N.b.*) 14 wks later. Percentages of fate-mapped cells analyzed on day 12 post-infection and compared to uninfected littermates (A). (B-D) Numbers and percentages of fate-mapped and non-fate-mapped ILC2s in lung (B), spleen (C), and mesenteric LN (D). (E) Percentages of fate-mapped ILC2s in BM. ILC2s gated as Lin^{-}IL-7Rα^{+}Thy1^{+}CD25^{+} (BM), Lin^{-}Thy1^{+}ST2^{+} (lung and spleen), or Lin^{-}IL-17RB^{+}KLRG1^{+} (mesenteric LN). Data

are pooled from multiple independent experiments and displayed as mean ± SEM of 8–9 mice.

KEY RESOURCES TABLE

REAGENT or RESOURCE	SOURCE	IDENTIFIER
Antibodies		
Anti-mouse Siglec-F AF647 (clone E50–2440)	BD Biosciences	Cat# 562680
Anti-mouse CD45 BUV395 (clone 30-F11)	BD Biosciences	Cat# 565967
Anti-mouse CD3 AF488 (clone 17A2)	BioLegend	Cat# 100210
Anti-mouse CD3 PB (clone 17A2)	BioLegend	Cat# 100214
Anti-mouse CD3 PE/Cy7 (clone 17A2)	BioLegend	Cat# 100220
Anti-mouse CD4 BV711 (clone RM4–5)	BioLegend	Cat# 100550
Anti-mouse CD5 BV421 (clone 53–7.3)	BioLegend	Cat# 100629
Anti-mouse CD8α PB (clone 53–6.7)	BioLegend	Cat# 100725
Anti-mouse/human CD11b PB (clone M1/70)	BioLegend	Cat# 101224
Anti-mouse CD25 BV605 (clone PC61)	BioLegend	Cat# 102036
Anti-mouse Thy1.2 BV785 (clone 30-H12)	BioLegend	Cat# 105331
Anti-mouse Gr-1 PB(clone RB6–8C5)	BioLegend	Cat# 108430
Anti-mouse NK-1.1 PB (clone PK136)	BioLegend	Cat# 108722
Anti-mouse CD49b PB (clone DX5)	BioLegend	Cat# 108918
Anti-mouse CD19 PB (clone 6D5)	BioLegend	Cat# 115523
Anti-mouse TER-119 PB (clone TER-119)	BioLegend	Cat# 116232
Anti-mouse CD11c PB (clone N418)	BioLegend	Cat# 117322
Anti-mouse TCR γ/δ BV421 (clone GL3)	BioLegend	Cat# 118120
Anti-mouse CD103 APC/Cy7 (clone 2E7)	BioLegend	Cat# 121431
Anti-mouse F4/80 PB (clone BM8)	BioLegend	Cat# 123124
Anti-mouse FcεRIα PB (clone MAR-1)	BioLegend	Cat# 134314
Anti-mouse NKp46 BV421 (clone 29A1.4)	BioLegend	Cat# 137612
Anti-mouse IL-17RB APC (clone 9B10)	BioLegend	Cat# 146308
Anti-mouse/rat/human ICOS APC (clone C398.4A)	BioLegend	Cat# 313510
Streptavidin APC	BioLegend	Cat# 405207
Anti-mouse EpCAM PerCP-Cy5.5	BioLegend	Cat# 118220
Anti-mouse PDGFRα APC	BioLegend	Cat# 135908
Anti-mouse Sca-1 BV711	BioLegend	Cat# 108131
Anti-mouse CD31 PE	BioLegend	Cat# 102407
Anti-mouse Podoplanin APC/Cy7	BioLegend	Cat# 127417
Anti-mouse Ki-67 FITC (clone SolA15)	eBioscience	Cat# 11–5698-82
Rat IgG2a kappa Isotype Control (eBR2a) FITC	eBioscience	Cat# 11–4321-80
Anti-human CD4 PE (clone RPA-T4)	eBioscience	Cat# 12–0049
Anti-mouse Gata-3 PE (clone TWAJ)	eBioscience	Cat# 12–9966-42
Anti-human CD4 APC (clone RPA-T4)	eBioscience	Cat# 17–0049
Anti-mouse KLRG1 PerCP-eF710 (clone 2F1)	eBioscience	Cat# 17–5893

REAGENT or RESOURCE	SOURCE	IDENTIFIER
Anti-mouse CD127 APC/eFluor780 (clone A7R34)	eBioscience	Cat# 47–1271-82
Anti-mouse ST2 Biotin (clone DJ8)	MD Biosciences	Cat# 101001B
Anti-mouse ST2 PE (clone DJ8)	MD Biosciences	Cat# 101001PE
Chemicals, Peptides, and Recombinant Proteins		
4',6-Diamidine-2'-phenylindole dihydrochloride (DAPI)	Roche	Cat# 10236276001
Tamoxifen	Sigma	Cat# T5648
rIL-33	Biolegend	Cat# 580504
Experimental Models: Organisms/Strains		
Mouse: wild-type: C57BL/6	The Jackson Laboratory	Stock# 000664
Mouse: *Arg1*-RFP-CreER^{T2}	(Fig. 1), this report	N/A
Mouse: R26R-EYFP: B6.129X1-*Gt(ROSA)26Sor*$^{tm1EYFP)Cos}$/J	The Jackson Laboratory	Stock# 006148
Mouse: Yarg: B6.129S4-*Arg1*^{tm1Lky}/J	The Jackson Laboratory	Stock# 015857
Mouse: Id2-CreER^{T2}: B6.129S(Cg)-*Id2*$^{tm1.1(cre/ERT2)Blh}$/J	The Jackson Laboratory	Stock# 016222
Mouse: R26R-RFP	E. Robey, H. Luche, and H. Fehling (Luche et al., 2007, Eur J Immunol)	N/A
Mouse: *Il7r*$^{-/-}$: B6.129S7-*Il7r*^{tm1Imx}/J	The Jackson Laboratory	Stock# 002295
Mouse: Red5: B6(C)-*Il5*$^{tm1.1(icre)Lky}$/J	The Jackson Laboratory	Stock# 030926
Mouse: Smart13: B6.129S4(C)-*Il13*$^{tm2.1Lky}$/J	The Jackson Laboratory	Stock# 031367
Mouse: Nur77-GFP	J. Zikherman (Zikherman et al., 2012, Nature)	N/A
Mouse: Id2-eGFP: B6.129S(Cg)-*Id2*$^{tm2.1Blh}$/ZhuJ	The Jackson Laboratory	Stock# 016224
Mouse: B6 Cd45.1: B6.SJL-*Ptprc*^{a} *Pepc*^{b}/BoyJ	The Jackson Laboratory	Stock# 002014
Nippostrongylus brasiliensis	UCSF (R. Locksley)	N/A
Oligonucleotides		
Rps17 (fwd) 5'-CGCCATTATCCCCAGCAAG-3'	Elim Biopharmaceuticals	N/A
Rps17 (rev) 5'-TGTCGGGATCCACCTCAATG-3'	Elim Biopharmaceuticals	N/A
Il33 (fwd) 5'-AAGACCAGGTGCTACTACGC-3'	Elim Biopharmaceuticals	N/A
Il33 (rev) 5'-CTTCTTCCCATCCACACCGT-3'	Elim Biopharmaceuticals	N/A
Tslp (fwd) 5'-CCCTTCACTCCCCGACAAAA-3'	Elim Biopharmaceuticals	N/A
Tslp (rev) 5'-CCTGAGTACCGTCATTTCTCTCA-3'	Elim Biopharmaceuticals	N/A
Il5 (fwd) 5'-CTCTGTTGACAAGCAATGAGACG-3'	Elim Biopharmaceuticals	N/A
Il5 (rev) 5'-TCTTCAGTATGTCTAGCCCCTG-3'	Elim Biopharmaceuticals	N/A
Il13 (fwd) 5'-CCTGGCTCTTGCTTGCCTT-3'	Elim Biopharmaceuticals	N/A
Il13 (rev) 5'-GGTCTTGTGTGATGTTGCTCA-3'	Elim Biopharmaceuticals	N/A
Software and Algorithms		
FlowJo v.10.5	FlowJo	flowjo.com
Prism v.7.0	GraphPad	graphpad.com
Cell Ranger	10X Genomics	10xgenomics.com

REAGENT or RESOURCE	SOURCE	IDENTIFIER
Loupe Cell Browser	10X Genomics	10xgenomics.com